THE JOURNAL OF PHYSICAL CHEMISTRY B
A JOURNAL OF THE AMERICAN CHEMICAL SOCIETY

pubs.acs.org/JPCB

Feature Article

# Mid-Infrared Photothermal Microscopy: Principle, Instrumentation, and Applications

*Published as part of The Journal of Physical Chemistry virtual special issue "Xiaoliang Sunney Xie Festschrift".*

Qing Xia, Jiaze Yin, Zhongyue Guo, and Ji-Xin Cheng*

Cite This: *J. Phys. Chem. B* 2022, 126, 8597−8613

Read Online

ACCESS | Metrics & More | Article Recommendations

**ABSTRACT:** Midinfrared photothermal (MIP) microscopy, also called optical photothermal infrared (O-PTIR) microscopy, is an emerging tool for bond-selective chemical imaging of living biological and material samples. In MIP microscopy, a visible probe beam detects the photothermal-based contrast induced by a vibrational absorption. With submicron spatial resolution, high spectral fidelity, and reduced water absorption background, MIP microscopy has overcome the limitations in infrared chemical imaging methods. In this review, we summarize the basic principle of MIP microscopy, the different origins of MIP contrasts, and recent technology development that pushed the resolution, speed, and sensitivity of MIP imaging to a new stage. We further emphasize its broad applications in life science and material characterization, and provide a perspective of future technical advances.

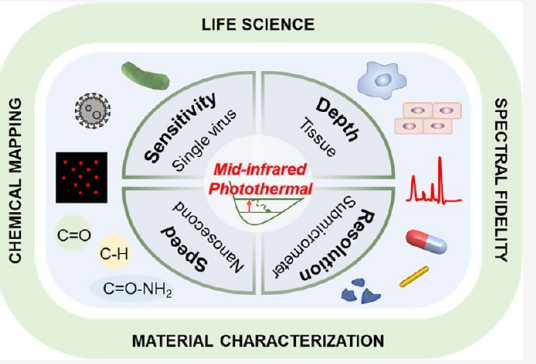


## 1. INTRODUCTION

Optical microscopy based on the light−matter interactions has been used for hundreds of years to magnify and resolve tiny objectives. Advances in optical imaging technology have revolutionized the way we perceive the world and improved our ability to study life and materials. Conventional optical microscopes, such as bright-field and phase microscopes, play an important role in cellular and molecular biology experiments, but lack molecular information.[1] For visualization of molecules, fluorescent labels have been widely used in biomedical research and demonstrated its capability of dynamic cellular imaging.[2,3] Although fluorescence microscopy shows three-dimensional (3D) imaging with high spatial resolution to nanometer scale,[4−6] high temporal resolution down to submillisecond scale,[7] and single-molecule sensitivity,[8] the lack of chemical information on the tagged molecules limits the functional analysis of cells or organelles.

Chemical microscopy based on intrinsic signals from chemical bond vibrations offers a way to overcome such limitations. Vibrational imaging methods offer intrinsic chemical selectivity based on spectroscopic signatures of chemicals. Raman spectroscopy, one of the cornerstones of molecular analysis, offers a way of mapping specific chemical bonds without labels. Spontaneous Raman microscopy offers submicron spatial resolution, but with a slow imaging speed.[9,10] By generating a much enhanced signal level, coherent anti-Stokes Raman scattering (CARS) or stimulated Raman scattering (SRS) microscopy[11] allowed video rate vibrational imaging of biological and pharmaceutical samples.[12,13]

However, either spontaneous or coherent Raman microscopy suffers from an extremely small Raman cross section (~$10^{-30}$ $cm^2$ $sr^{-1}$), which limits its ultimate detection sensitivity. Infrared (IR) spectroscopy is complementary to Raman spectroscopy. Importantly, IR absorption offers 8 orders of magnitude larger cross section (~$10^{-22}$ $cm^2$ $sr^{-1}$) that enables adequate sensitivity. Based on IR spectroscopy, the Fourier transform infrared (FTIR) microscopy has been developed for spatially resolved chemical information on biological samples.[14−16] Despite the well-established modality and wide applications, FTIR imaging is limited to spectral acquisition over a large bandwidth, even when only a few bands are of interest.[17] Quantum cascade laser (QCL)-based discrete frequency IR imaging can select specific vibration bands, providing rapid chemical imaging of a specimen.[17] However, due to the diffraction limit of long excitation wavelengths, the spatial resolution of IR imaging usually ranges from 3 to 30 $\mu$m.[18] Such poor resolution greatly limits the chemical analysis of single microorganisms or subcellular structures. To tackle

**Received:** August 14, 2022
**Revised:** October 7, 2022
**Published:** October 26, 2022

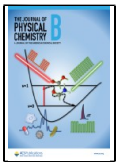







https://doi.org/10.1021/acs.jpcb.2c05827
*J. Phys. Chem. B* 2022, 126, 8597−8613

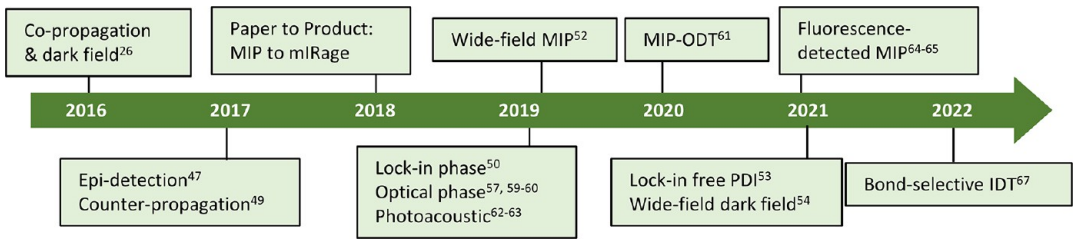


**Figure 1.** Timeline showing major developments and achievements in mid-infrared photothermal (MIP) imaging. ODT: optical diffraction tomography. PDI: photothermal dynamic imaging. IDT: intensity diffraction tomography.

these challenges, a near-field scanning approach has been developed to provide nanoscale chemical imaging,[19−22] such as atomic force microscopy infrared (AFM-IR) spectroscopy. With an AFM tip, AFM-IR can detect and map IR-induced thermal expansion with nanoscale resolution (~20 nm),[23] but with a slow acquisition speed on the order of tens of minutes per frame.[24] Additionally, although AFM-IR has been applied to liquid samples with the equipment of a total internal reflection IR prism to overwhelm the influence of water,[21,25] complex setup and procedures make them unsuitable for routine use. It remains difficult to conduct AFM-IR analysis of living systems in an aqueous environment.

Recently developed mid-infrared photothermal (MIP) microscopy[26] surpasses the fundamental limitations encountered by FT-IR and AFM-IR in both resolution and liquid specimen application. In an MIP microscope, a visible probe beam detects the photothermal chemical contrast induced by a vibrational absorption. When the wavelength of the pump mid-IR beam is tuned to the absorption peak of the sample, the thermal effect will lead to a local temperature change and consequently thermal expansion, pressure wave emission, change of refractive index, and change of Grüneisen parameter.[27] By measuring the corresponding divergence variation in the copropagating probe beam, a photothermal chemical contrast can be acquired. Thus, the submicron resolution is reached according to the diffraction limit of the probe wavelength in the visible region. Furthermore, as MIP microscopy measures absorption indirectly, the background caused by nonresonant water absorption is minimal due to the large heat capacity and small temperature increase of water.[28] Compared to direct absorption measurements in IR microscopy, MIP imaging opens a new window for chemical analysis of living cells in liquid environment.

## 2. HISTORICAL DEVELOPMENT OF MID-INFRARED PHOTOTHERMAL MICROSCOPY

Since the photothermal deflection measurements reported in the 1980s and the 1990s,[29,30] photothermal spectroscopy has been a ultrasensitive technique for measuring optical absorbance and estimating concentrations of nanoparticles and nonfluorescent molecules in solvents.[31−33] Photothermal spectroscopy employs a nonlinear signal generation via a pump−probe mechanism, in which a pump beam is served as the heating source and a probe beam detects the local refractive index change induced by the heat release from sample absorption.[31] Benefiting from the high signal-to-noise ratio (SNR) of no background absorption and the low photon noise of the probe beam, visible photothermal microscopy based on the electronic or plasmonic absorption has been developed.[34] Photothermal detection of single absorbers, such as single nanoparticles or single molecules, has been demonstrated.[35−38]

With the advantages of high-sensitivity and label-free nature, photothermal-based methods were extended from the visible to the IR region in both microscopy and spectroscopy. Lee et al.[39] demonstrated a scanning photothermal IR microscope by mechanically chopping an IR beam, through which lipid droplets in fixed 3T3-L1 preadipocytes were chemically imaged at resolution of 1.1 $\mu$m.[40] In a conference proceeding, Furstenberg et al.[41] employed a tunable QCL pump beam to a reflection photothermal microscope and acquired IR spectra of small crystals. Technological progress has also been made in photothermal spectroscopy. Erramilli and Sander reported nonlinear photothermal spectroscopy by using a QCL pump beam and nonlinear Zharov splitting in 50-$\mu$m homogeneous liquid crystal layers.[42−44] In conference proceedings, Mërtiri et al. showed photothermal imaging of dried bird brain tissue with the use of a mid-IR pump, near-IR probe, and a silicon objective lens.[45] Li et al. demonstrated photothermal imaging of 1.1 $\mu$m polystyrene beads at the single particle level in water, glycerin, and carbon disulfide.[46]

In 2016, the Cheng group reported a high-performance QCL-based MIP microscope and demonstrated, for the first time, 3D bond-selective imaging of living cells and organisms at a spatial resolution of 0.6 $\mu$m.[26] Through a dark-field geometry and a resonant amplifier, an unprecedented detection limit of C═O bond at 10 $\mu$M was reached. In 2017, the Cheng group reported an epi-detected MIP microscope that enables noncontact material characterization.[47] Via an effective academic−industry partnership, the MIP microscope has been quickly commercialized into a product mIRage, announced by Photothermal Spectroscopy Corp (Santa Barbara, CA, USA) in 2018.[48] Continuous technical innovations by academic laboratories have enabled higher sensitivity and higher resolution in MIP imaging. Major recent developments and achievements are summarized in Figure 1. To push the spatial resolution limit, the Hartland group[49] demonstrated a counter-propagation system with a 532 nm probe beam and a high numerical aperture water immersion objective, and achieved a spatial resolution of 0.3 $\mu$m. By using the phase-sensitive lock-in detection, the Sander group[50] provided higher contrast and enhanced spatial resolution for bond-selective imaging of a single weak absorber. By harnessing interferometric scattering with confocal configuration, the Cheng group[51] pushed the MIP sensitivity limit to single virus detection. To boost the imaging speed, Cheng and Shakouri.[52] developed a wide-field MIP microscope by sensing the transient photothermal effect induced by absorption of single mid-IR pulses and allowed ultrafast chemical imaging of thin polymer films at 1000 frames per second. Very recently, the Cheng group reported lock-in free photothermal dynamic imaging (PDI) with signal digitization and match filtering.[53] This


https://doi.org/10.1021/acs.jpcb.2c05827
J. Phys. Chem. B 2022, 126, 8597−8613

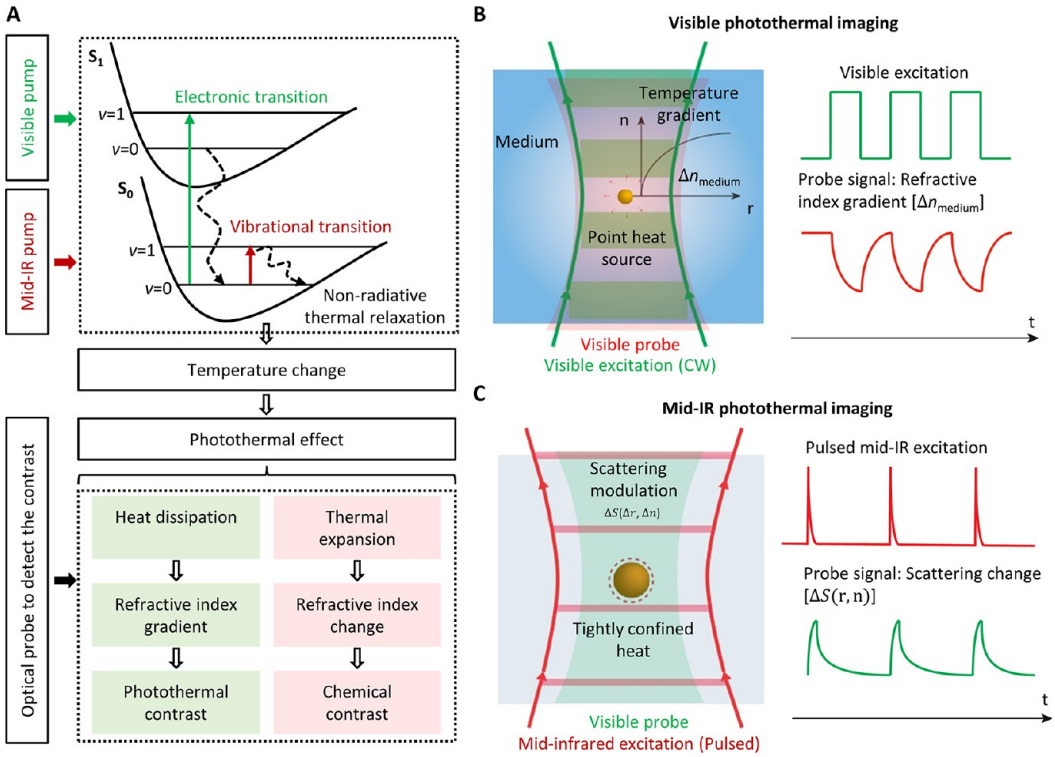


**Figure 2.** Comparison of visible and mid-IR photothermal imaging. (A) Molecular energy level diagram and block diagram show the visible/IR absorption-induced photothermal contrast. (B) Detection mechanism of visible photothermal microscopy: a modulated continuous wave (CW) is used as the pump source (green) for inducing periodical heating. The nanoabsorber (yellow) serves as point heat sources, leading to a local temperature and refractive index gradient ($\Delta n_{medium}$) of surrounding medium (blue). A probe beam (red) is used to detect the thermal lens. Adapted from ref 76. Copyright 2014 AIP Publishing. (C) Principle of scattering-based MIP microscopy: A pulsed mid-IR laser, used as the pump (red), induces a temperature rising at the absorber (orange), causing the local change of thermal expansion ($\Delta r$), refractive index ($\Delta n$), and thus the intensity of scattering from the absorber. A probe beam (green) is used to detect the photothermal effect. In this condition, the samples are big nanoparticles and the heating source is above the resolution of the probe.

method increased the imaging speed by 2 orders of magnitude and realized 4-fold enhancement of SNR.

In addition to the progress in resolution and sensitivity improvement, various mechanisms of MIP detection have been explored. The MIP signal is mainly detected by optically probing the scattering from a sample, including dark-field scattering,[26,54,55] interferometric scattering,[51,56] and optical phase.[57−61] Other than the scattering-based contrast, the photoacoustic (PA) signal[62,63] and fluorescence[64−66] have been exploited to indicate the difference between IR on and IR off states. The Cheng,[57] Ideguchi,[58,60] and Bhagavar[59] groups simultaneously appreciated the use of optical phase to sense the MIP effect, which also brings chemical information into a phase image. The Lihong Wang group pushed the MIP spatial resolution to 260 nm by employing ultraviolet-excited PA detection of MIP signals.[62] The Ideguchi[61] and Cheng[67] groups realized depth-resolved MIP imaging of biological samples using optical diffraction tomography (ODT) and intensity diffraction tomography (IDT), respectively. The Cheng[64] and Simpson[65] groups had two back-to-back JACS publications showing the mid-IR modulation of fluorescence, which not only increases the specificity of MIP but also provides a 100-fold enhancement in modulation depth compared to the modulation of scattering intensity.

Meanwhile, combining MIP with other techniques opens more opportunities. For example, the Cheng group[68] integrated confocal Raman spectroscopy to MIP imaging, which not only provides complementary chemical information by full-spectrum Raman analysis but also shares submicron spatial resolution by MIP microscopy. The Klementieva group[69] developed a multimodal spectroscopic imaging approach with the combination of MIP and X-ray fluorescence, which shows the chemical imaging of trace elements and molecular structures in neurons. With these advances in technology, MIP imaging has found broad applications in biology and material science, such as biomolecular mapping,[68,70] metabolic activities monitoring,[26,63] bacterial antibiotics response,[71] single virus detection[51] and material characterization.[72−74] In this feature article, we review the principle, recent technical advances and versatile applications in the biomedical and material sciences.

## 3. PRINCIPLE OF MIP MICROSCOPY

In MIP microscopy, the chemical contrast originates from vibrational absorption induced thermal effect. When a molecule is excited by a pump beam, it quickly returns back to the ground state with energy release through nonradiative thermal relaxation. The photothermal effect leads to a local temperature increase and then the changes of the sample's optical and physical properties.[31] Such changes are detected by a visible probe beam in an MIP microscope (Figure 2A). Below we compare MIP to visible photothermal microscopy and then discuss the thermal dynamics in time and space.

**3.1. Comparison of Visible and Mid-IR Photothermal Imaging.** Visible photothermal microscopy is one kind of optical microscopy that gauges electronic absorption with extremely high sensitivity (Figure 2A).[37,38,75,76] For visible


https://doi.org/10.1021/acs.jpcb.2c05827
J. Phys. Chem. B 2022, 126, 8597−8613

photothermal imaging, the absorbers usually have an extremely small radius (~nm), such as gold nanoparticles, chromophores, or single molecules. As electronic absorption provides a strong light−matter interaction between photons and nanoabsorbers, most of them have a large absorption cross section. Visible photothermal microscopes employ a continuous wave (CW) modulated by acousto-optic modulator (AOM) as the pump source for inducing periodical heating. As the heating beam spot is much larger than the nanoabsorbers, absorbers can serve as point heat sources, leading to a local temperature change of surrounding medium (Figure 2B). With the formed medium temperature gradient within the diffraction limit, visible photothermal microscopy can map the single nanoabsorbers by measuring the refractive index gradient of the medium ($\Delta n_{medium}$) with a visible probe.[34]

While in MIP microscopy a pulsed mid-IR laser is used as the pump beam, which can provide tightly confined heat and induce a high temperature rise at the absorber (Figure 2C).[26,27] As the local temperature is periodically modulated, the thermal relaxation induced by vibrational absorption causes local change of thermal expansion ($\Delta r$) and refractive index ($\Delta n$) of the absorber itself. The absorbers often have a comparable size with the visible probe beam and, thus, can serve as the signal source in MIP imaging. In most cases, the scattering intensity modulation is adopted to generate the chemical contrast.[77,78] It is worth noting that all the photothermal detection originates from the perturbation of the probe beam, but the contrast mechanism could be attributed to a specific process based on the relative size between the heat source and probe focus. In photothermal imaging of nanoparticles with a much smaller size than the probe focus, or where the excitation focus is smaller than the probe focus, the contrast would be attributed to thermal lensing. In this condition, the absorber can be simplified as an ideal point heat source and its origin scattering field is negligible. Absorbed energy needs to be dissipated to the medium to form the refractive index gradient and cause the perturbation of the probe. On the other hand, if the heat source itself is above the resolution of the probe, the photothermal modulation alternates its scattering field directly, and the probe is perturbed without waiting for formation of the thermal lensing in the medium. For those excitation volumes larger than the probe resolution, the direct modulation of sample refractive index is dominant.

With the rapid development of MIP microscopy, various detection schemes (see section 4) in full bloom bring this bond-selective chemical imaging technique to a new level.

### 3.2. Photothermal Dynamics in Time and Space.

*3.2.1. Transient Heat Conduction of a Sphere Particle in a Uniform Medium.* The mid-IR modulated photothermal effect arises from the local heating. When the analyte is irradiated with a very short mid-IR pulse (<1 $\mu$s), one can calculate the transient heat conduction of the sphere objects with the fundamentals of heat and mass transfer.[79] The transient heat conduction of the particle depends on the opto-physical properties of the particle itself and the surrounding environment. Assuming that the object's diameter $D$ is held at a temperature ($T_1$, $t < 0$) and is embedded within an infinite medium of uniform temperature ($T_2$) (Figure 3), the heat conduction follows Newton's law of cooling:

$$mC_s\frac{dT}{dt} = -q_{diss} \tag{1}$$

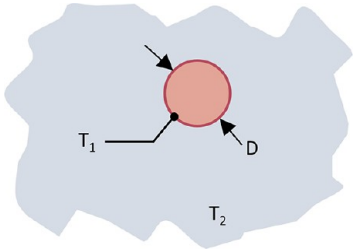


**Figure 3.** A model of transient heat conduction for a sphere particle placed in a uniform medium. The object (red) with diameter $D$ is held at a temperature ($T_1$, $t < 0$) and is embedded within an infinite medium (gray) of uniform temperature ($T_2$) at $t = 0$.

where $m$ is the object mass, $C_s$ is the object specific heat capacity, and $q_{diss}$ is the heat dissipation source. For a sphere particle,

$$q_{diss} = 2\pi kD(T(t) - T_2) \tag{2}$$

where $k$ is the thermal conductivity of the medium and $T(t)$ is the time-dependent object temperature. When eq 2 is integrated into eq 1 and the differential equation is solved, we can get

$$\frac{T(t) - T_2}{T_1 - T_2} = \exp\left[-\left(\frac{2\pi kD}{mC_s}\right)t\right] \tag{3}$$

Thus, the decay constant $\tau$ in analogy to an RC circuit is

$$\tau = \left(\frac{1}{2\pi kD}\right)(mC_s) = R_tC_t \tag{4}$$

where $R_t$ is the resistance to heat transfer and $C_t$ is the lumped thermal capacitance.

To validate this transient heat conduction model, we choose a poly methyl-methacrylate (PMMA) spherical particle as an example (Table 1), which has $C_s$ = 1460 [J/(kg*K)] and

**Table 1. Calculated Decay Constant of $D$ = 500 nm PMMA Particles in a Homogeneous Medium**

| Medium | Thermal conductivity $k$ at 20 °C/ W*m$^{-1}$*K$^{-1}$ | Decay constant $\tau_t$/ns |
|---|---|---|
| Air | 0.024 | 1500 |
| Glycerol | 0.26 | 135 |
| Water | 0.6 | 60 |

density $\rho$ = 1180 [kg/m$^3$]. For particles embedded in a homogeneous medium, the decay constant is proportional to $D^2$ and scale inversely with $k$ according to eq 4. For PMMA particles in air, we obtain the decay constant $\tau_t$ = 6000 ns for $D$ = 1000 nm and $\tau_t$ = 1500 ns for $D$ = 500 nm, according to $k_{air}$ = 0.024 [W/(m*K)]. In real experimental cases, the particle is placed on a substrate such as silicon or calcium fluoride. In this complex condition, the decay constant is hard to be evaluated by this simple model. The simulated decay constant for $D$ = 500 nm PMMA in the air but on a silicon substrate can be calculated by COMSOL Multiphysics, which is $\tau_t$ = 430 ns according to our previous work.[27] It is much smaller than the one completely surrounded by the air ($\tau_t$ = 1500 ns). Thus, due to the large thermal conductivity ($k_{silicon}$ = 1.5 × 10$^5$ [W/(m*K)]), silicon wafer is often used as the substrate for MIP imaging, which can reduce the heat accumulation and avoid overheating of the sample between IR pulses. When the medium is with better


https://doi.org/10.1021/acs.jpcb.2c05827
J. Phys. Chem. B 2022, 126, 8597−8613

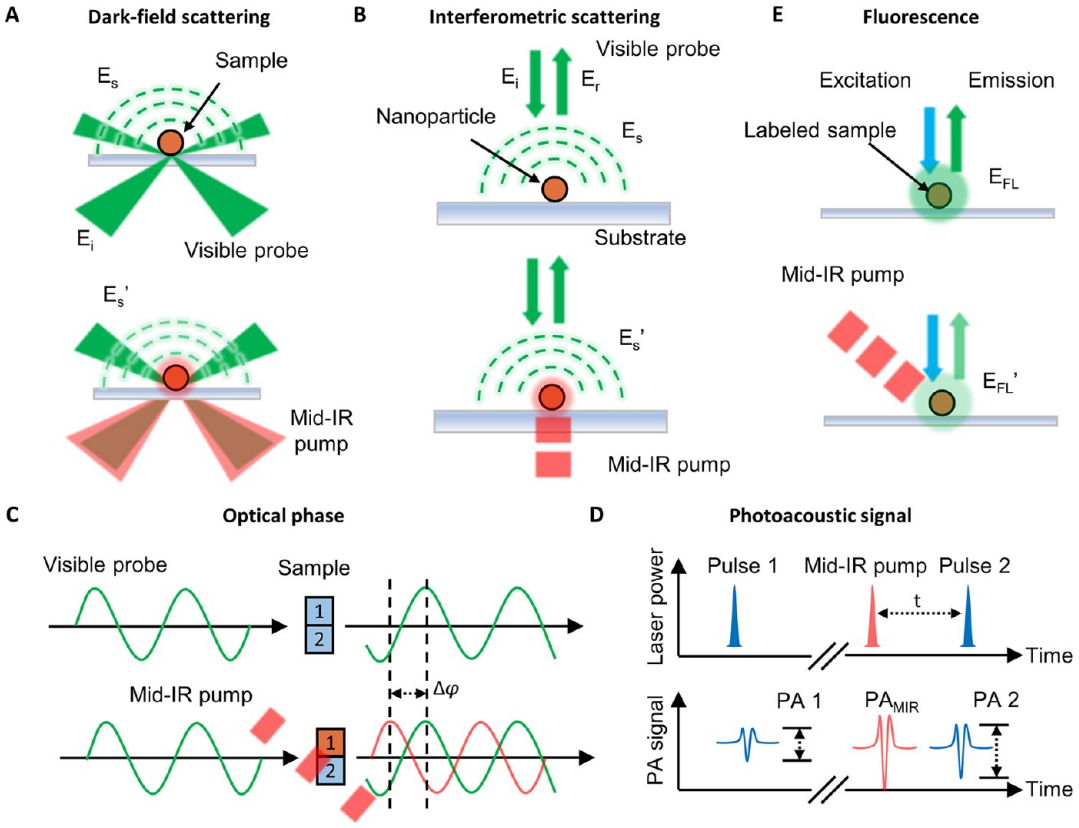


**Figure 4.** MIP signal detection mechanisms. (A) Dark-field scattering-based MIP imaging. As mid-IR pump beam is modulated, the size and local refractive index change induce the modulation of the scattering field $E_s$ of the sample. The scattering modulation of the probe field ($E_i$) is maximized by a dark-field illumination geometry. (B) Interferometric scattering-based MIP detection. With a reference field $E_r$ to amplify the weak scattering signal, MIP imaging probes the interferometric reflectance change from the sample, which is the coherent sum of $E_r$ and $E_s$. (C) Optical phase-based MIP detection. The photothermal effect induces a refractive index change of the sample, which further alters the optical path length in the probe beam. The MIP contrast is detected by measuring the transient change in phase shift $\Delta\varphi$ induced by vibrational absorption. Adapted with permission from ref 57. Copyright 2019 Springer Nature Limited. (D) Photoacoustic-detected MIP. Two pulsed probe beams generate PA signals at the state without and with mid-IR pump. The difference between the two PA signals indicates the magnitude of the vibrational absorption by the sample. Adapted with permission from ref 62. Copyright 2019 Springer Nature Limited. (E) Fluorescence-detected MIP. Thermosensitive dyes are chosen as probes of the photothermal effect due to the strong thermal dependence of emission efficiencies. The pulsed mid-IR pump beam induces a temperature rise around the dye, which subsequently modulates the fluorescence emission $E_{FL}$.

thermal conductivity than air, a faster heat conduction can also be reached, such as $\tau_t$ is 135 ns in glycerol and 60 ns in water, respectively (Table 1). In principle, the photothermal modulation period is limited by the thermal decay constant, which defines the highest modulation frequency for complete heat dissipation and further determines the speed of MIP imaging.

*3.2.2. Thermal Diffusion in Space.* For MIP imaging application to materials, cells, and organisms, the thermal diffusion of the medium could cause a heated background and compromise the spatial resolution. In a uniform medium, the heat transfer rate is proportional to the temperature gradient

$$\Phi = -kA\nabla T(x, t) \tag{5}$$

where $\Phi$ is the heat flux, $k$ is the thermal conductivity, and $A$ is the unit area. The 1-D solution is

$$T(x, t) = T_0 - T_0\mathrm{erf}\left(\frac{x}{2\sqrt{\alpha t}}\right) \tag{6}$$

where, for $t \geq 0$, erf is the error function and $\alpha$ is thermal diffusivity.

Thus, the thermal diffusion length can be defined as

$$L = 2\sqrt{\alpha t} \tag{7}$$

which gives the distance at which the amplitude of the heat flux reduces by $e$ times from its sample's surface value at $x = 0$.

If we assume $t = \tau = 240$ ns for a PMMA particle of 1 $\mu$m diameter, the calculated thermal diffusion length is $L$= ~200 nm in water. Such short thermal diffusion length sets the foundation for submicron spatial resolution in MIP imaging. Meanwhile, water absorption of the visible probe beam is negligible and mid-IR light can penetrate water up to ~100 $\mu$m based on the absorption coefficient in the1000 to 3000 $cm^{-1}$ window, which allows MIP imaging of living cells and small organisms cultured in a medium.

## 4. DIFFERENT MIP MODALITIES

The mainstream of MIP detection mechanism is based on the optical scattering of the samples. Three different strategies have been used for scattering-based MIP imaging: (i) dark-field scattering[26,54,80,81] (Figure 4A), (ii) interferometric scattering[49,51,52,56,68] (Figure 4B), and (iii) optical phase[57−59,61] (Figure 4C). In parallel, other detection mechanisms have been explored, including (iv) PA signal[62,63,82] (Figure 4D) and (v) fluorescence intensity[64,65] (Figure 4E).



https://doi.org/10.1021/acs.jpcb.2c05827
J. Phys. Chem. B 2022, 126, 8597−8613

**4.1. Dark-Field Scattering-Based MIP Imaging.** Compared to the visible photothermal imaging, MIP detection suffers from the small cross section of mid-IR absorption and large focal volume of the pump beam. To detect small signals in the scattering background, dark field geometry (Figure 4A) is deployed by Zhang et al. to maximize the scattering contrast modulation in the probe beam and reduce the background noise.[26] In this configuration, the probe beam propagates through the sample via the dark-field objective. When the pump beam is modulated, the temperature rise at the IR focus greatly changes the local refractive index, which further alters the propagation of the probe beam. This scattering perturbation can be sensitively detected by the dark-field geometry, which allows MIP imaging of live cells and organisms with submicron spatial resolution and microsecond-scale pixel dwell time.[26] In 2017, Sullenberger et al.[81] reported wide-field MIP modulation based on dark-field detection of Mie scattering. In this work, a QCL pump induces a periodic change in the particle's optophysical properties and a CW 532 nm laser probes the scattering of the particles (Figure 5A). The magnitude of the

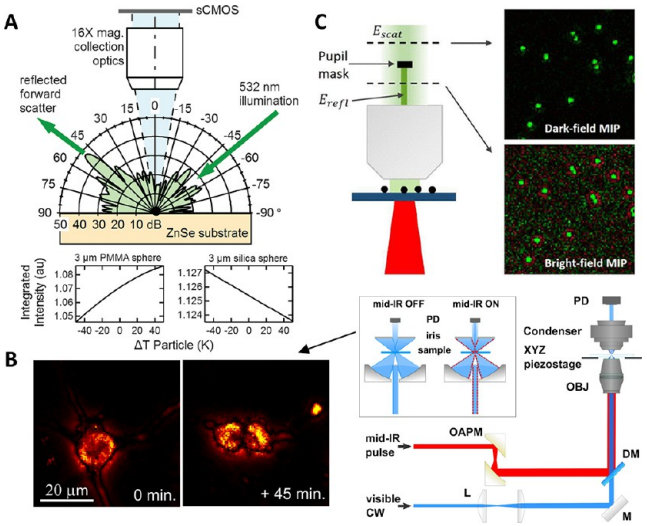


**Figure 5.** Technical advances of dark-field scattering-based MIP imaging. (A) MIP modulation based on Mie scattering shows temperature change induced integrated scattering intensity of a 3 $\mu$m PMMA particle. Reprinted with permission from ref 81. Copyright 2017 Optica Publishing Group. (B) Cellular dynamics of living brain cells observed by MIP microscopy with the deployment of an incubation chamber. Adapted with permission from ref 80. Copyright 2019 American Chemical Society. (C) Dark-field MIP microscopy in a wide-field manner. A pupil engineering strategy attenuated the reflected background light and enabled 6-fold enhancement of SNR. Reprinted from ref 54. Copyright 2021 American Chemical Society.

Mie scattering oscillation is found to be proportional to particle absorption and pump intensity, which enabled concurrent spatial and spectral discrimination of individual 3 $\mu$m PMMA and silica spheres. By using the same configuration reported by Zhang et al.,[26] Lim et al.[80] deployed an incubation chamber on the microscope to maintain the culture conditions for MIP imaging of living cells. In this work, MIP imaging was used to monitor cytoplasmic protein distributions and cellular dynamics of living brain cells such as oligodendrocytes and neurons (Figure 5B). Via a pupil engineering strategy, Zong et al.[54] realized dark-field MIP imaging in a wide-field manner, providing 6-fold signal-to-background noise ratio improvement (Figure 5C).

**4.2. Interferometric Scattering-Based MIP Detection.** When it comes to the subwavelength bionanoparticles, such as a single virus, a single exosome, or even a single protein, the elastic scattering intensity of these nano-objects scales with the sixth power of the particle size. The weak scattering from the sample makes them indistinguishable from the background in elastic scattering-based MIP imaging. To address this challenge, interferometric scattering-based MIP detection has been developed by using a reference field to amplify the weak scattering signal and push the sensitivity down to a single virus.[51] In this model, MIP imaging probes the interferometric reflectance change from the sample, and the camera captures the intensity signal from the coherent sum of reference and scattered fields (Figure 4B). With the interference with a stronger reference field, the weakly scattered light from the nano-object is greatly enhanced. By detection of interferometric scattering in a confocal configuration, interferometric MIP not only enjoys a reduced size dependence of optical contrast (scaling with the third power of the particle size)[83] but also enables chemical imaging down to nanoparticles.[51]

Interferometric MIP imaging is generally implemented by using a counterpropagating geometry of pump and probe beams first reported by Li et al.,[49] in scanning or wide-field manners. In the confocal scanning manner, a tunable mid-IR pump beam is focused at the sample via a Cassegrain objective and a CW visible probe beam is focused at the same spot with a high numerical aperture (NA) refractive objective (Figure 6A). The detection signal arises from the interference between the particle scattering and the reflected probe beam. With the deployment of a high NA objective for the probe system, MIP microscopy can reach the spatial resolution of 0.3 $\mu$m and showed the ability to chemically image 100 nm polystyrene beads[49] and single viral particles.[51] With a similar counterpropagating geometry, Bai et al.[52] developed a widefield interferometric MIP microscope and allowed ultrafast chemical imaging at the speed of 1250 frames per second (Figure 6B). With the synchronization of exposure frames with a modulated mid-IR pump and pulsed visible probe, time-resolved MIP imaging via a regular camera was achieved. However, since the low power density of IR pump and weak photothermal signal of single bionanoparticles, wide-field MIP also faces challenges in detection limit and quantitative analysis. Via substrate design, Yurdakul et al.[56] utilized a 70 nm silicon nitride/silicon layered substrate to increase interferometric contrast by reducing the background and enhancing the scattered field (Figure 6C). Such technical improvements advance the MIP microscopy toward high-resolution and high-throughput spectroscopic imaging of individual bionanoparticles including viruses, exosomes, and protein assemblies.

**4.3. Optical Phase-Based MIP Detection.** Transparent samples, such as biological cells, can affect the probe beam in terms of optical phase delay.[84] This provides a new way for MIP imaging of transparent specimens. As shown in Figure 4C, when the probe beam propagates through the sample, a phase image can be acquired via the interference with a reference beam. The photothermal effect induces a refractive index change of the sample, which alters the optical path length via the thermo-optic effect. MIP contrast is then acquired by measuring the transient change in phase shift induced by vibrational absorption, which can further provide a spectral information with scanning the IR wavelength.[57] Besides the


https://doi.org/10.1021/acs.jpcb.2c05827
J. Phys. Chem. B 2022, 126, 8597−8613

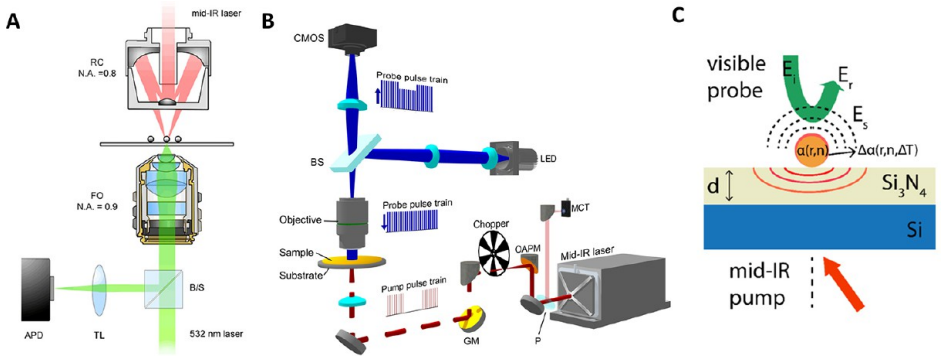


**Figure 6.** Technical advances in interferometric scattering-based MIP imaging. (A) Counter-propagation MIP detection of particles on a substrate. A mid-IR pump beam focused at the sample via a Cassegrain objective and a visible probe beam focused at the same spot with a high numerical aperture (NA) refractive objective allows MIP detection of the interference between the particle scattering and the reflected probe beam. Reprinted from ref 49. Copyright 2017 American Chemical Society. (B) Wide-field MIP with a virtual lock-in camera strategy. A modulated mid-IR pump and a pulsed visible probe are synchronized with the exposure frames of a regular camera, pushing the time resolution to submillisecond level. Reprinted with permission from ref 52. Copyright 2019 American Association for the Advancement of Science. (C) Substrate-modified interferometric MIP microscopy. A 70 nm silicon nitride/silicon layered substrate is used to increase interferometric contrast by reducing background and enhancing the scattered field. Reprinted from ref 56. Copyright 2021 IOP Publishing.

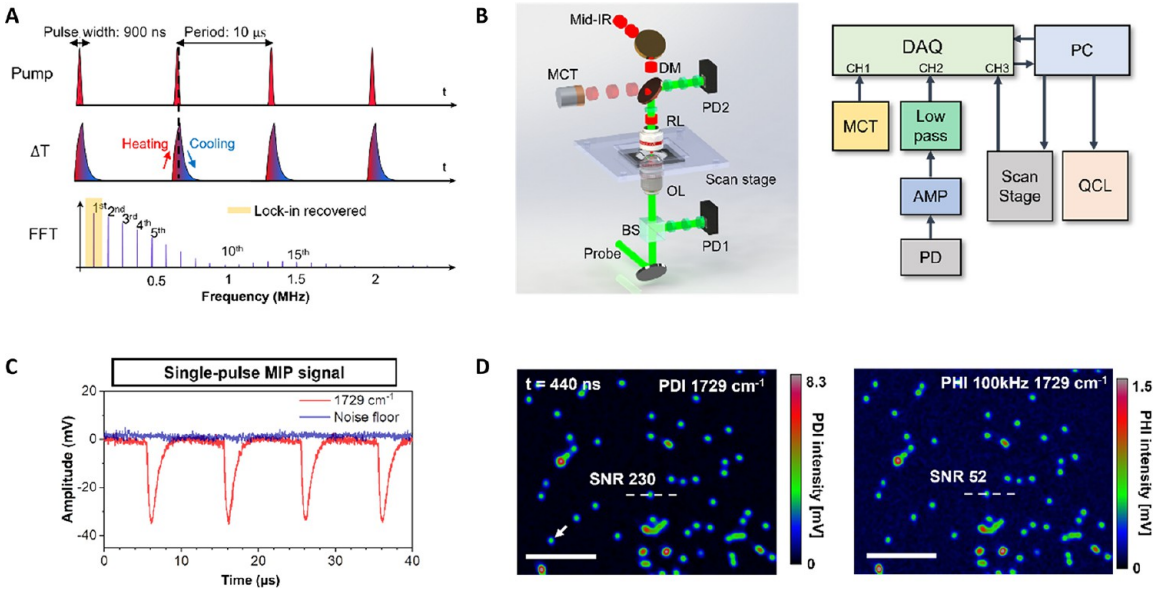


**Figure 7.** A lock-in free wideband data acquisition system for transient photothermal dynamics detection. (A) Simulation of local temperature modulation under a pulsed IR excitation. The absorber has a decay constant of 400 ns; the IR source has a repetition rate of 100 kHz and a pulse duration of 900 ns. (B) PDI setup schematics and electronics diagram. A pulsed mid-IR beam is focused on the sample with a reflective objective lens (RL). Backscattered probe photons are collected with a 50/50 beam splitter (BS), forward scattered probe photons are collected by the reflective objective and separated by a dichroic mirror (DM). Probes are collected and sent to silicon photodiodes (PD) connected with a wideband voltage amplifier. A high-speed data acquisition (DAQ) card is used to collect photodiode signal after voltage amplifier (AMP). (C) Raw photothermal dynamics signal acquired from 500 nm diameter polymer particles under the IR excitation at 1729 $cm^{-1}$. (D) PDI image of 300 nm diameter polymer particles at 1729 $cm^{-1}$ excitation and conventional MIP image acquired with the lock-in amplifier in the same field of view. PDI shows over 4 times SNR improvement for single particle detection. Adapted with permission from ref 53. Copyright 2021 Springer Nature Limited.

adoption of interference to amplify the weak scattering signal, optical phase-based MIP modalities also show the advantages in imaging specimen that are with similar refractive index with the medium. Cheng, Popescu and co-workers reported a bond-selective phase microscope by integration of pulse IR excitation and a diffraction phase microscope.[57] Ideguchi's group independently developed an MIP microscope with optical phase as readout, which can quantify the sample-specific optical-phase-delay with chemical sensitivity.[60,85] By combining the quantitative signal with machine learning, Schnell[59] et al. advanced the phase-based MIP microscopy toward applications across the spectrum of biomedical science.

**4.4. Photoacoustic-Detected MIP.** The local temperature change can also be measured through PA detection of the Grüneisen coefficient Γ that is linearly proportional to the PA signal and is sensitive to local temperature with a dependency of $d\Gamma/dT$ by 4%/K. To provide high spatial resolution and uniform PA signal over the whole sample, pulsed ultraviolet laser was used as the probe in the PA-detected MIP microscopy.[62] Here, a pulsed mid-IR pump beam excites the sample to generate PA signals at IR on and off states as shown


https://doi.org/10.1021/acs.jpcb.2c05827
J. Phys. Chem. B 2022, 126, 8597−8613

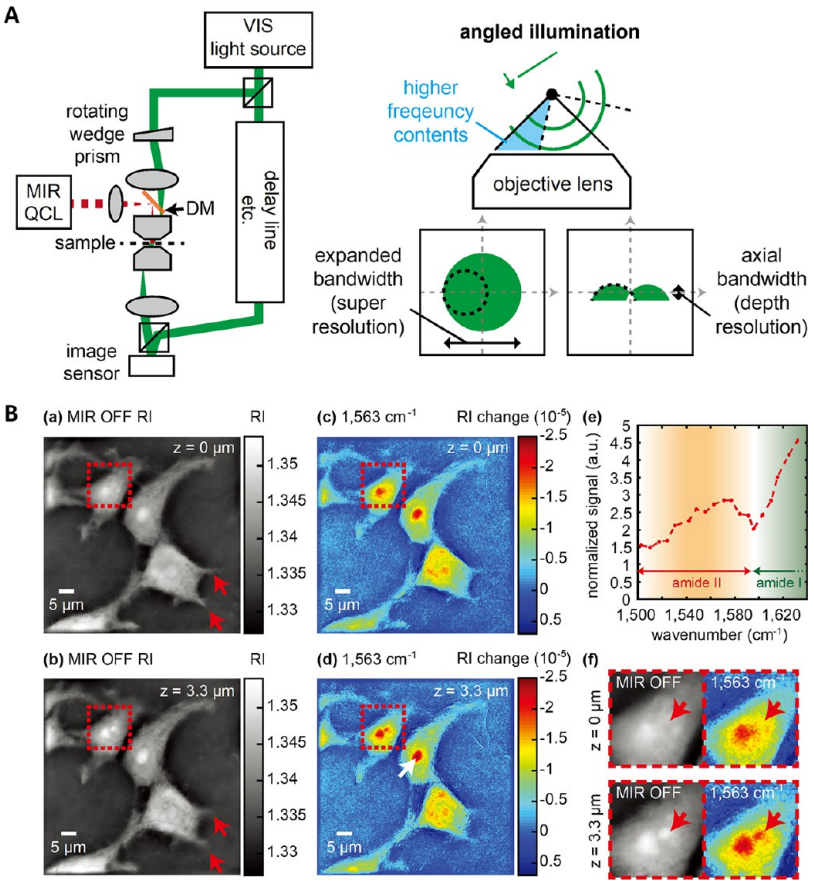


**Figure 8.** Technical advances in mid-infrared photothermal tomography. (A) Depth-resolved ODT detection for chemically cellular imaging. The probe beam (green) is split into two paths to create the Mach−Zehnder off-axis interferometer and illuminates the sample at various incident angles by a rotating wedge prism. (B) By adding the pulsed IR pump beam (red), the reconstructed tomography allows (a, b) refractive index (RI) and (c, d) MIP detection of the fixed HEK293 cells at different axial planes. (e) The MIP spectrum shows the resonant of protein amide II band (1563 $cm^{-1}$) in the nucleolus (white arrow in (d)). (f) Zoom-in images in (a)−(d) (red-square regions) show the depth-resolving capability of the nucleolus. Reprinted from ref 61. Copyright 2020 Optical Society of America. ODT: optical diffraction tomography.

in Figure 4D. The difference between two PA signals can indicate the magnitude of the vibrational absorption that is linked to the temperature rise.[62] With the employment of an ultraviolet laser, photoacoustic MIP imaging can provide high-resolution, high-contrast chemical imaging of fresh biological samples. As the lateral resolution is determined by the wavelength of probe beam, photoacoustic MIP imaging can reach a high spatial resolution of 250 nm according to the diffraction limit of ultraviolet wavelength. In addition, ultraviolet light not only is transmissive in water[86] but also has a high absorption of most biomolecules.[87] This provides a suppressed water background and an imaging contrast of the biological samples in the liquid environment. Moreover, the ultraviolet probe beam can propagate in thick samples,[88] providing a way to image biological tissues without thin slicing.

**4.5. Fluorescence-Detected MIP.** For scattering-based MIP detection, the photothermal effect induces a small scattering modulation, typically on the order of $10^{-4}$/K, due to the small thermal expansion and thermo-optic coefficient of the samples. While in wide-field MIP imaging, the scattering intensity at each pixel is limited by the well depth of a CMOS camera. Thus, such small scattering modulation depth limits the SNR especially in the wide-field detection.[52] As an alternative, fluorophores have a strong thermal dependence of emission efficiencies (~1%/K), which is about 100 times larger than the thermally induced scattering modulation. Based on this principle, fluorescence-detected MIP microscopy has been independently developed by the Cheng group[64] and Simpson group,[65] offering improved image quality and video rate chemical imaging speed. In a typical fluorescence-based MIP microscope, thermosensitive fluorescent dyes are chosen as probes of the photothermal effect (Figure 4E).[64] After the sample is stained with a selected thermosensitive fluorophore, the fluorescence emission efficiency can be modulated by the temperature change induced by a pulsed mid-IR pump beam. With a highly increased modulation depth, the wide-field MIP imaging speed can be improved by 2 orders of magnitude up to video rate.[64] In addition, the excitation and emission light of fluorescence are at different wavelengths without any interference patterns. Taken together, fluorescence-based MIP imaging provides both suppressed-background and improved image quality. Furthermore, the fluorescence labels offer specific information on the biomolecules, which augments the specificity of MIP imaging.

**4.6. Lock-in Free Photothermal Dynamic Imaging.** To detect the small modulation on the probe beam, the lock-in amplifier has been used to extract the signal at the pump laser modulation frequency. Such a single frequency filtering technique is ideal for analyzing sinusoidal signals or signal with a 50% duty cycle. In addition, the modulation frequency should be chosen where the background noise is minimized for reaching high SNR. However, these two conditions are not


https://doi.org/10.1021/acs.jpcb.2c05827
J. Phys. Chem. B 2022, 126, 8597−8613

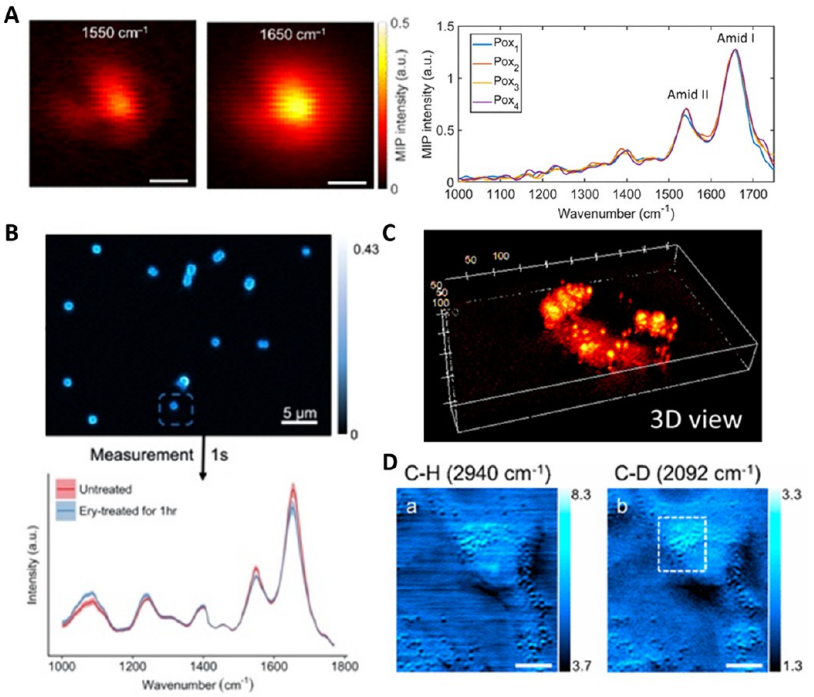


**Figure 9.** Biological applications of MIP microscopy ranging from single viruses, single bacteria to single mammalian cells. (A) MIP imaging of one single poxvirus at amide I (1650 $cm^{-1}$) and amide II (1550 $cm^{-1}$) bands and MIP spectra of four single poxviruses at the fingerprint region. Reprinted with permission from ref 51. Copyright 2021 American Chemical Society. (B) MIP imaging of single *S. aureus* at amide I (1650 $cm^{-1}$) and averaged single-cell MIP spectra showing different fingerprint spectra of untreated and erythromycin-treated (1 h) *S. aureus* cells. Reprinted with permission from ref 71. Copyright 2020 American Chemical Society. (C) The reconstructed 3D view from depth-resolved MIP imaging at the 1750 $cm^{-1}$ C═O band of a live PC-3 cell shows the individual lipid droplets. Reprinted from ref 26. Copyright 2016 American Association for the Advancement of Science. (D) MIP imaging of $d_{31}$-palmitic acid treated A549 lung cancer cells. MIP imaging at 2940 $cm^{-1}$ reveals C−H rich lipid and protein contents while MIP imaging at 2092 $cm^{-1}$ (C−D peak) shows the distribution of $d_{31}$-palmitic acid metabolites. Reprinted with permission from ref 55. Copyright 2017 American Chemical Society.

satisfied in the case of MIP imaging. In MIP, nanosecond pulsed excitation is usually employed for maintaining high spatial resolution and high contrast.[27] The local temperature of a sample under impulse excitation is illustrated in Figure 7A, which is composed of a transient temperature jump followed by an exponential decay. Successful extraction of such transient signal requires information from the fundamental frequency and the higher-order harmonics simultaneously which is beyond the capability of lock-in detection. In addition, the IR repetition rate is limited to below hundreds of kilohertz due to the mandatory cooling period.[53] The 1/f noise from the probe light source is dominant in this frequency region, resulting in a degraded SNR.

To overcome the obstacles, a lock-in free detection scheme termed photothermal dynamics imaging (PDI) for sensing the transient photothermal dynamics was developed by the Cheng group.[53] In this method, a wide-band acquisition system is employed instead of narrow-band filtering. As illustrated in Figure 7B, the intensity modulation signal on the probe beam is detected with a fast photodiode and directly digitized after wide-band amplification. With nanosecond-scale temporal resolution, the photothermal dynamics are revealed as shown in Figure 7C. By utilizing the signal in higher order harmonics where system noise is reduced, a significant SNR improvement than in the case of lock-in detection is achieved (Figure 7D). With such sensitivity, PDI enables photothermal detection under single pulse excitation, which largely boosts the speed of MIP imaging. Furthermore, captured photothermal dynamics reveal the thermal property of samples, bringing a new dimension of information together with IR absorption for sample scrutinization, including sensing the microenvironment, differentiating small signals from the water background.[53]

Collectively, with the temporal resolution in a nanoseconds scale, PDI provides the tool for investigating complex photothermal processes such as nonlinear heating effect[89,90] and superimposed thermal dissipation[53] at submicron spatial resolution.

**4.7. Midinfrared Photothermal Tomography.** To provide depth-resolved spectroscopic detection of biological samples, MIP-based chemical phase microscopy has been developed to enable quantitative volumetric chemical imaging. The Ideguchi group presented MIP quantitative phase microscopy with ODT for depth-resolved molecular vibrational imaging.[61] In ODT, a probe beam is split into two paths to create an incident and a reference wave by the configuration of a Mach−Zehnder off-axis interferometer. A rotating wedge prism is used to provide multiangle tomographic measurements (Figure 8A). By applying a pulsed IR beam to ODT, phase-based MIP images are reconstructed from the modulated scattered light fields with diffraction effect, which enables volumetric chemical analysis of complex and fragile biological samples. The reconstructed tomography allows refractive index and MIP detection of the fixed HEK293 cells at different axial planes, which shows the depth-resolving capability of the nucleolus in the cell (Figure 8B).

More recently, the Cheng and Tian groups reported a bond-selective intensity diffraction tomography (BS-IDT) scheme for a noninterferometric volumetric MIP imaging of cells and


https://doi.org/10.1021/acs.jpcb.2c05827
J. Phys. Chem. B 2022, 126, 8597−8613

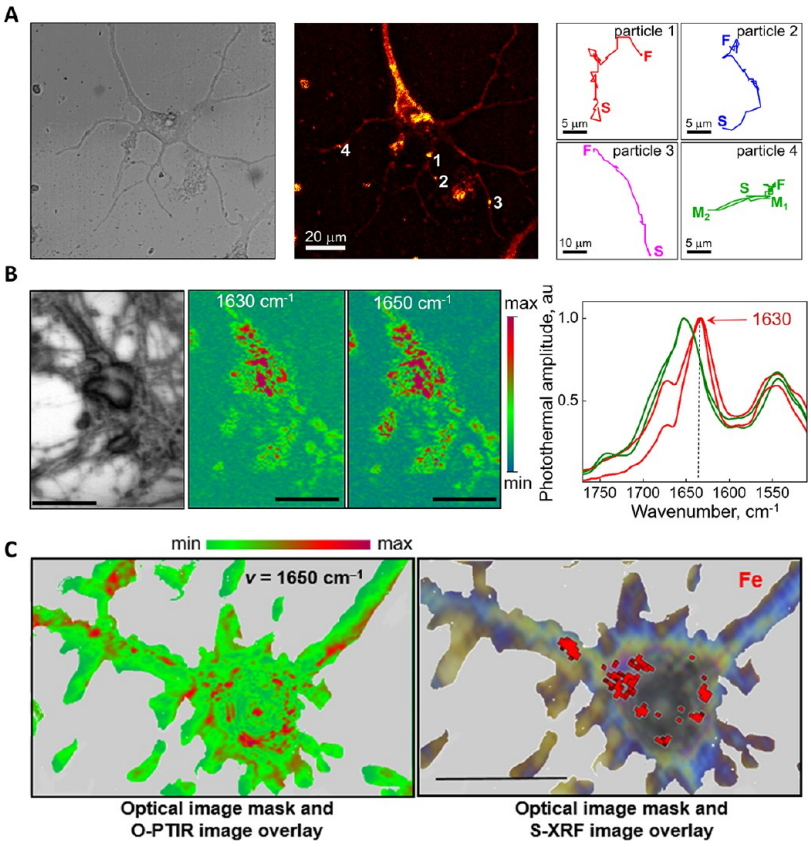


**Figure 10.** Applications of MIP microscopy in protein analysis of living neurons. (A) Bright-field and MIP images for live neurons are shown and long-term (4 h, 340 s time interval) MIP imaging allows tracking of four MIP signals associated with the bidirectional and slow transport of axonal protein along the dendrite branches. Reprinted with permission from ref 80. Copyright 2019 American Chemical Society. (B) O-PTIR imaging of APP-KO primary neuron incubated with synthetic A$\beta$(1−42) revealed the $\beta$-sheet elevated aggregation by O-PTIR mapping at 1630 and 1650 cm$^{-1}$. Reprinted from ref 93. Copyright 2020 John Wiley & Sons, Inc. (C) Co-registered O-PTIR image (at 1650 cm$^{-1}$ with red as max and green as min) and S-XRF image (in red) enables correlative study of protein structures and trace elements directly in APP-KO primary neuron incubated with synthetic A$\beta$(1−42). Reprinted from ref 69. Copyright 2021 Springer Nature Limited. S-XRF: synchrotron-based X-ray fluorescence.

organisms.[67] A customized nanosecond pulsed laser ring array is integrated with the time-gated pump pulses in BS-IDT, which enables the acquisition of transient 3D refractive index variations at microsecond time scale.

## 5. BROAD APPLICATIONS

MIP spectroscopic imaging allows molecular recognition at submicron spatial resolution, which provides new insights for chemical study in biomedical and material science. Since the demonstration of a high-performance MIP microscope in 2016, this technology was quickly commercialized into a product mIRage in 2018. MIP microscopy, also called optical photothermal infrared (O-PTIR) microscopy, is emerging as a valuable tool for life analysis, environmental monitoring, and material characterization. Below we highlight some exciting applications.

**5.1. Bond-Selective Imaging in Life Science.** MIP has enabled multiscale applications in life science, ranging from single viruses, single bacteria, single mammalian cells, sliced tissues, to whole organisms. MIP detection of a single virus has been demonstrated in both poxvirus and vesicular stomatitis virus at the fingerprint region (Figure 9A).[51] The dominant spectral features are attributed to the amide I band at 1650 cm$^{-1}$ and the amide II band at 1550 cm$^{-1}$, indicating the viral proteins. Limited by the optical resolution, the MIP images of single poxvirus at both wavenumbers are shown as high contrast diffraction-limited spots. The rich chemical information at the fingerprint region offers a new idea to differentiate viral particles based on variations in biocomposition; this bond-selective imaging and spectral analysis opens a new way for subtyping biological nanoparticles in a label-free manner.

MIP has enabled metabolic imaging of bacteria at the single-cell level, in both the fingerprint[68,70,71] and high wavenumber region.[49] The bacterial metabolic response to antibiotics (erythromycin) has been revealed by the MIP spectral change in single *S. aureus* (Figure 9B).[71] Rapid characterization of antibiotic response has been achieved by in situ spectroscopic analysis of single bacteria. This provides accurate and comprehensive information on the physiological state of individual bacteria and can further reveal the heterogeneity within an isogenic population. Additionally, MIP can also be used to study specific metabolic activities by identifying the isotope-labeled compounds uptake.[70]

When it comes to the complex organelles inside mammalian cells, MIP microscopy shows the high-performance chemical imaging of specific components of living cells. Bond-selective analysis of C═O bond[26] and C−H band[55,57] were demonstrated to study the lipid droplets in single cancer cells. Label-free 3D mapping of lipid droplets inside a single living cancer cell has been further demonstrated (Figure 9C).[26] Combined with isotope labeling, the fatty acid metabolism was visualized in cancer cells at the C−D band (Figure 9D).[55] To study the


https://doi.org/10.1021/acs.jpcb.2c05827
J. Phys. Chem. B 2022, 126, 8597−8613

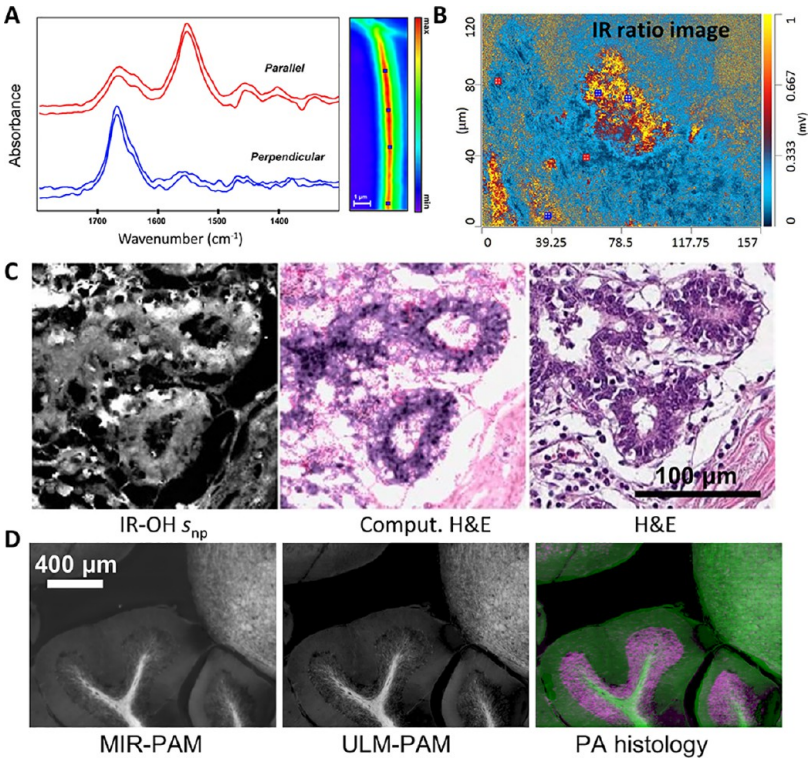


**Figure 11.** Applications of MIP microscopy in histology. (A) O-PTIR spectra from single tendon fibril show different amide I and II profiles with the fibril parallel or perpendicular to IR laser polarization. O-PTIR imaging at 1655 $cm^{-1}$ in perpendicular orientation shows the fibril to be no more than 500 nm across. Reprinted from ref 95. Copyright 2020 MDPI. (B) O-PTIR image ratio map of 1037/1660 $cm^{-1}$ (phosphate/amide I) enable evaluation of stimulatory effects of peptides on osteogenesis and biomineralization. Reprinted from ref 96. Copyright 2021 Elsevier. (C) Digital histopathology based on IR absorption. IR absorption image at 1550 $cm^{-1}$ on the left and computed H&E image using the stainless staining approach in the middle compared to the H&E image of adjacent tissue section on the right. scale bar 100 $\mu$m. Adapted with permission from ref 59. Copyright 2020 National Academy of Science. (D) For a 300 $\mu$m thick cerebellum section from a freshly fixed mouse brain, mid-infrared photoacoustic microscopy (MIR-PAM) image with MIR at 3420 nm (peak absorption of myelin lipids) provides structural information on nerve fibers or bundles while ultraviolet-localized MIR photoacoustic microscopy (ULM-PAM) image reveals nerve fibers or bundles at higher resolution and low water background. Further overlaid with a photoacoustic microscopy (UV-PAM) image with UV wavelength around 224 nm for nucleic acid, the PA histology show both the myelin in green and nucleic acid in purple. Reprinted from ref 62. Copyright 2019 Springer Nature Limited.

metabolic activity in living cells, the MIP-induced acoustic signal was used to monitor the lipids, proteins, and carbohydrates in 3T3-L1 adipocytes during lipid droplet formation.[63] The high sensitivity of MIP to biochemical variations has enabled differentiation between lung cancer cells and normal cells.[91] Local biochemical variability was also demonstrated within single, healthy red blood cells via MIP imaging.[92]

Label-free MIP imaging is very sensitive to protein amounts and secondary structures, thus opening new possibilities of dynamic protein analysis in living neurons. Real-time MIP imaging of oligodendrocytes was reported to investigate cellular dynamics during division, apoptosis, and migration. The intercellular protein-rich vesicle transportation on the axons of a live neuron was also observed (Figure 10A).[80] As protein aggregation is associated with many neurodegenerative diseases and often with enriched $\beta$ sheet components in the secondary structure, MIP offers new opportunities for studying protein aggregation and its structure in vivo. Klementieva et al.[93] revealed a $\sim$ 20 $cm^{-1}$ red shift of the amide I peak in amyloid fibrils in the MIP spectrum and achieved label-free identification of amyloid aggregation at the subcellular level by comparing the MIP intensity ratio between an $\alpha$ helix and $\beta$ sheet (Figure 10B). Furthermore, the structural polymorphism of amyloid protein aggregations in neurons has also been revealed by variations in the amide I band. The capability of identifying the protein secondary structure and lipid-rich bodies on the submicron scale has also been demonstrated in live cancer cells.[94] With the combination of synchrotron-based X-ray fluorescence nanoimaging techniques, Gustavsson et al.[69] coregistered the trace element composition information and revealed that iron clusters colocalize with elevated amyloid $\beta$-sheet structures and oxidized lipids in primary AD-like neurons (Figure 10C).

With technological advancement and commercialization, MIP microscopy also shines in the field of chemical histology. Using an mIRage system, Bakir et al.[95] realized spectroscopic detection and chemical imaging of collagen down to the single fibril level (Figure 11A). Rahmati et al.[96] visualized the distribution of phosphate and amine content via MIP imaging and evaluated the conformational changes of peptides and their effects on osteogenesis and biomineralization (Figure 11B). Combined with machine learning, Schnell et al.[59] obtained full slide IR absorption images of an unstained breast tissue microarray slide and developed algorithms to realize the automated histopathologic segmentation and generation of computationally stained images (Figure 11C). With the employment of PA detection, MIP microscopy can provide label-free histology analysis and offer rich chemical and structural information on tissue samples.[62,82] Shi et al.[62]


https://doi.org/10.1021/acs.jpcb.2c05827
J. Phys. Chem. B 2022, 126, 8597−8613

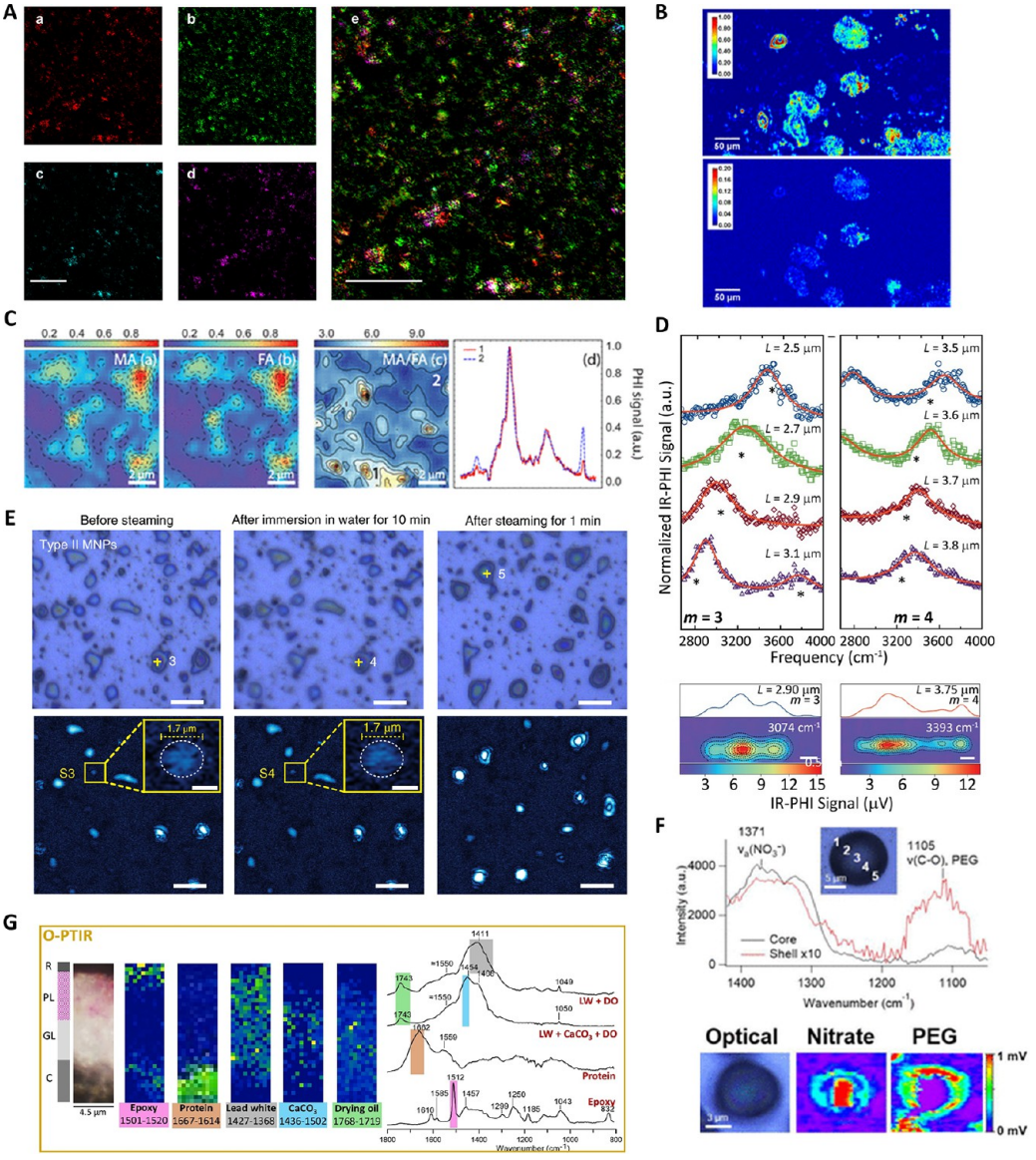


**Figure 12.** Applications of MIP microscopy in material science. (A) Epi-MIP image of a Tylenol tablet at (a) 1413, (b) 1502, (c) 1656, (d) 1750 $cm^{-1}$, and (e) overlaid image of (a–d) show the distribution of active pharmaceutical ingredients acetaminophen (green) and three most abundant excipients corn starch(red), poly vinylpyrrolidone (PVP in cyan) and sodium starch gycolate (SSG in magenta) respectively. Reprinted with permission from ref 47. Copyright 2017 American Chemical Society. (B) O-PTIR imaging at the characteristic absorption peaks (1003 $cm^{-1}$) of the highly explosive PETN reveal its distribution within fingerprints for forensic purposes. Reprinted with permission from ref 98. Copyright 2020 American Chemical Society. (C) MIP imaging reveals the spatial heterogeneities in cation-specific compositions in mixed cation perovskite films. Reprint with permission from ref 99. Copyright 2018 American Chemical Society. (D) MIP spectra of single, high aspect ratio Au nanowires between 2800 and 4000 $cm^{-1}$ reveals a series of resonances. The MIP images show the spatial distribution of the nanowire absorption. Reprint with permission from ref 72. Copyright 2020 National Academy of Science. (E) The submicrometer resolution of O-PTIR (at 1747 $cm^{-1}$) enables the visualization and characterization of micro(nano)plastics (imides-containing particles) released from the heated silicone-rubber baby teats. Reprinted with permission from ref 73. Copyright 2021 Springer Nature Limited. (F) O-PTIR reveals the core–shell morphology of liquid–liquid phase-separated particles with aerodynamic diameters <400 nm containing ammonium nitrate primarily in the core and PEG primarily in the shell. Reprinted with permission from ref 102. Copyright 2020 American Chemical Society. (G) O-PTIR imaging distinguishes the compositions across the thin layers of the stratigraphy for an extremely small fragment extracted from Van Gogh's painting. Reprinted with permission from ref 103. Copyright 2021 Wiley-VCH GmbH.

demonstrated high-resolution and high-contrast chemical imaging of myelin and nucleic acid in thick brain slices (Figure 11D).

**5.2. Chemical Imaging in Material Science.** In material analysis, the application of MIP microscopy spans energy systems, environment, and cultural heritage, including characterization of drugs, nanoparticles, nanocomposites, microplastics, polymers, and environmental pollutants.

Providing rich chemical information and submicron resolution, MIP microscopy is an emerging tool for in situ, nondestructive chemical analysis of bulk or nanoscale drugs. The Cheng group demonstrated first application of MIP microscopy in mapping intracellular drug distribution.[26] With the development of an epi-detected MIP microscope,[47] Li et al. showed active pharmaceutical ingredients and excipients visualization in a Tylenol tablet (Figure 12A). Distribution of


https://doi.org/10.1021/acs.jpcb.2c05827
J. Phys. Chem. B 2022, 126, 8597–8613

drugs and excipients in single pharmaceutical inhalation aerosols was also mapped using a commercial microscope mIRage.[97] It is expected that the capability of MIP in rapid, label-free drug formulation characterization will promote research in pharmaceutical science and advance the pharmaceutical industry. With the high-performance in chemical mapping and spectroscopic detection, MIP has also shown potential in rapid detection of highly explosive materials. For example, Banas et al.[98] has reported the rapid detection of exogenous high-explosive substances deposited within fingerprints, such as pentaerythritol tetranitrate (PETN) for forensic purposes (Figure 12B).

MIP has also proven to be a useful tool in the energy field. Kuno and co-workers revealed the correlation between solar cell performance and cation composition.[74,99] Large compositional spatial heterogeneities in mixed cation perovskite films were visualized via MIP mapping of local cation-specific compositional distributions (Figure 12C).[99] The authors further investigated the bias-induced cation migration of perovskite and suggested a cation instabilities suppressed strategy in hybrid perovskites to improve the solar cell stability.[74] In the plasmonic field, with IR spectroscopic mapping of 2.5−3.8-$\mu$m-long gold nanowires (NWs) (Figure 12D), the resonances of the NWs were assigned to different Fabry−Pérot modes and the finite element simulations matched the experimental results very well.[72] The components were mapped at the interface of the bioplastics, polyhydroxyalkanoate, and polylactic acid laminate sample. A complex spatial distribution of the constituents was found in the laminate, rather than a simple binary system.[100] Independently, by providing chemical property information, MIP microscopy was applied to explain the in situ fibrosis mechanism of polytetrafluoroethylene (PTFE) composites during the one-step extrusion process.[101]

With submicron spatial resolution, MIP has demonstrated applications in analysis and/or detection of contaminants, such as microplastics and other environmental contaminants in air or water. By using the mIRage system, Su et al.[73] revealed the release of micro(nano)plastics from silicone-rubber baby teats after steam etching and chemical modification of the surface (Figure 12E). By quantifying the direct exposure of bottle-fed infants to surface-active microplastics, it was estimated that over 0.66 million elastomer-derived microplastics may be ingested by a one-year-old baby. Via MIP microscopy, the distribution of chemical species within atmospheric particles was mapped at the single sub- and supermicrometer particle level (Figure 12F), providing both physical and chemical properties of single atmospheric aerosols.[102]

With nanoscale spatial resolution and offering comparable spectroscopic information as FTIR, MIP microscopy has also become a promising tool in cultural heritage. The reduced amount of extracted sample and the nondestructive nature of MIP measurements help preserve the integrity of artwork while providing a complete chemical characterization of the components. The detection of geranium lake pigments and analysis of the stratigraphy were achieved in a Van Gogh painting[103] (Figure 12G), and the distribution of chemical phases was mapped in a 19th-century painting.[104] Providing information on nanocomposition, MIP is expected to advance the understanding of chemical processes in oil painting and guide the conservation of historical paintings.

## 6. SUMMARY AND OUTLOOK

MIP microscopy is an emerging tool for high-resolution imaging of chemicals in biological and material samples. In this review, we have discussed various detection methods, technology developments, and broad applications in life science and material science. Since the first report of high-performance chemical imaging of living cells and organisms at submicron resolution,[26] MIP microscopy has evolved in various ways. On the detection side, various methods including interferometric scattering,[51,56] optical phase,[57−61] lock-in phase,[50] PA detection,[62,63] fluorescence detection,[64−66] signal digitization,[53] and computational tomography[61,67] significantly improved the performance and broadened the application field. Meanwhile, advances are made in pushing the imaging resolution, speed, and sensitivity of MIP to the next stage. For examples, high spatial resolution of 300 nm has been achieved with a counter-propagation system.[49] Ultrafast imaging of 1250 frames/s has been reached on a wide-field manner.[52] Detection sensitivity down to a single virus has been realized via detection of interferometric scattering in a confocal configuration.[51] MIP microscopy has been widely used for mapping lipids, proteins, and carbohydrates in unstained live cells, monitoring metabolic activities, and mapping the distribution of specific molecules in various materials.

Although MIP microscopy has shown significant impact in life science and material characterization, more work is needed to improve the technology and expand the pool of applications. Looking into the future, we envision the following innovations in pump source, probe detection, and contrast enhancement. (i) For pump source, improvement in the pulse energy, pulse duration, repetition rate, and wavelength range of IR lasers can enhance the sensitivity and speed of MIP microscopy. Current MIP imaging utilizes a narrow-band IR laser to excite single absorption bands and usually requires a long time for overlapped band analysis. Reduction in laser tuning time between wavelengths will enable ultrafast hyperspectral MIP imaging. (ii) For probe detection, with the recently developed single pulse digitization method,[53] video rate and hyperspectral MIP imaging of living cells are expected. (iii) Contrast enhancement approaches such as interferometric detection[51,56] and plasmon resonance enhancement can push the MIP detection of small bionanoparticles in high-throughput.

On the application side, the boost in imaging speed and spectral information will enable more in-depth analysis in life science and material characterizations. (i) With the capability of chemical imaging at subcellular resolution, the MIP technique has the potential to provide a metabolic imaging platform for in situ characterization of lipid or protein metabolism in cells and brain organoids. (ii) With video rate MIP imaging, the dynamics of different cellular components can be tracked within a few seconds in a label-free manner. (iii) With ultrafast hyperspectral MIP imaging, complicated band analysis could be performed, such as protein secondary structure decomposition and isotope incorporation quantification. Additionally, rapid chemical analysis of unknown species in a high-throughput manner can be realized by the ultrafast hyperspectral imaging. (iv) For physiological and biochemical phenomena in live cells, chemical probes with mid-IR absorbance hold promise for multiplexed imaging in many biological events and signaling networks. MIP probes based on alkyne or nitrile tags are expected to provide high-resolution mapping of multiple enzyme activities at the subcellular level. (v) As MIP



https://doi.org/10.1021/acs.jpcb.2c05827
J. Phys. Chem. B 2022, 126, 8597−8613

microscopy is highly compatible with fluorescence, MIP imaging can benefit from the high specificity of widely used fluorescent probes for more targeted chemical analysis.

Finally, as increasing MIP modalities were developed and extensive applications were achieved, a rigorous theoretical framework should be established to explore the photothermal signal generation, such as the anticipated point-spread functions for the different MIP imaging modes. A deeper understanding of the origin of photothermal contrast will pave the way for further improvements of the technique to surpass current sensitivity and resolution.

## AUTHOR INFORMATION


### Corresponding Author

**Ji-Xin Cheng** − *Department of Electrical and Computer Engineering, Boston University, Boston, Massachusetts 02215, United States; Photonics Center and Department of Biomedical Engineering, Boston University, Boston, Massachusetts 02215, United States;* orcid.org/0000-0002-5607-6683; Email: jxcheng@bu.edu

### Authors

**Qing Xia** − *Department of Electrical and Computer Engineering, Boston University, Boston, Massachusetts 02215, United States; Photonics Center, Boston University, Boston, Massachusetts 02215, United States;* orcid.org/0000-0002-5939-2972

**Jiaze Yin** − *Department of Electrical and Computer Engineering, Boston University, Boston, Massachusetts 02215, United States; Photonics Center, Boston University, Boston, Massachusetts 02215, United States*

**Zhongyue Guo** − *Photonics Center and Department of Biomedical Engineering, Boston University, Boston, Massachusetts 02215, United States*

Complete contact information is available at: https://pubs.acs.org/10.1021/acs.jpcb.2c05827


### Notes

The authors declare no competing financial interest.

### Biographies

**Dr. Qing Xia** is a postdoctoral associate at Boston University. She received her B.S. degree in Chemistry from Nanjing Normal University, China. She earned her Ph.D. in Analytical Chemistry from Nanjing University, China. Her research is focused on advancement of mid-infrared photothermal microscopy and its applications in spectroscopic detection of single bionanoparticles and single molecules.

**Jiaze Yin** is currently a PhD candidate at Boston University in the Departments of Electrical and Computer Engineering. He received his B.S. degree in Biomedical Engineering from Beihang University. With a concentration in electrical engineering, his research is developing the data acquisition system combined with digital signal processing for photothermal detection and designing the optics system for realizing high-speed chemical imaging.

**Zhongyue Guo** is currently a third year PhD student in Biomedical Engineering at Boston University. She received her B.S. degree in Biomedical Engineering from Beihang University, China. Her research is focused on mid-infrared photothermal microscopy and its applications in protein aggregation and secondary structural analysis in living cells, starting with yeast as the eukaryotic model system.

**Professor Ji-Xin Cheng** is a faculty member associated with Departments of Electrical and Computer Engineering, Biomedical Engineering, Physics, and Chemistry at Boston University. Cheng joined Purdue University in 2003 as an Assistant Professor in the Weldon School of Biomedical Engineering and Department of Chemistry, promoted to Associate Professor in 2009 and Full



https://doi.org/10.1021/acs.jpcb.2c05827
J. Phys. Chem. B 2022, 126, 8597−8613

Professor in 2013. He joined Boston University as the Inaugural Theodore Moustakas Chair Professor in Photonics and Optoelectronics in the summer of 2017.

## ■ ACKNOWLEDGMENTS

This work is supported by R35GM136223 and R33CA261726 to J.X.C.

## ■ DEDICATION

This feature article is dedicated to "Xiaoliang Sunney Xie Festschrift" for his 60th birthday.

## ■ REFERENCES

(1) Mertz, J. *Introduction to optical microscopy*; Cambridge University Press: 2019.
(2) Gonçalves, M. S. T. Fluorescent labeling of biomolecules with organic probes. *Chem. Rev.* **2009**, *109* (1), 190−212.
(3) Dean, K. M.; Palmer, A. E. Advances in fluorescence labeling strategies for dynamic cellular imaging. *Nat. Chem. Biol.* **2014**, *10* (7), 512−523.
(4) Huisken, J.; Swoger, J.; Del Bene, F.; Wittbrodt, J.; Stelzer, E. H. K. Optical sectioning deep inside live embryos by selective plane illumination microscopy. *Science* **2004**, *305* (5686), 1007−1009.
(5) Rust, M. J.; Bates, M.; Zhuang, X. Sub-diffraction-limit imaging by stochastic optical reconstruction microscopy (STORM). *Nat. Methods* **2006**, *3* (10), 793−796.
(6) Betzig, E.; Patterson, G. H.; Sougrat, R.; Lindwasser, O. W.; Olenych, S.; Bonifacino, J. S.; Davidson, M. W.; Lippincott-Schwartz, J.; Hess, H. F. Imaging intracellular fluorescent proteins at nanometer resolution. *Science* **2006**, *313* (5793), 1642−1645.
(7) Diebold, E. D.; Buckley, B. W.; Gossett, D. R.; Jalali, B. Digitally synthesized beat frequency multiplexing for sub-millisecond fluorescence microscopy. *Nat. Photonics* **2013**, *7* (10), 806−810.
(8) Qu, X.; Wu, D.; Mets, L.; Scherer, N. F. Nanometer-localized multiple single-molecule fluorescence microscopy. *Proc. Natl. Acad. Sci. U.S.A.* **2004**, *101* (31), 11298−11303.
(9) Puppels, G. J.; de Mul, F. F. M.; Otto, C.; Greve, J.; Robert-Nicoud, M.; Arndt-Jovin, D. J.; Jovin, T. M. Studying single living cells and chromosomes by confocal Raman microspectroscopy. *Nature* **1990**, *347* (6290), 301−303.
(10) Haka, A. S.; Volynskaya, Z.; Gardecki, J. A.; Nazemi, J.; Lyons, J.; Hicks, D.; Fitzmaurice, M.; Dasari, R. R.; Crowe, J. P.; Feld, M. S. In vivo margin assessment during partial mastectomy breast surgery using Raman spectroscopy. *Cancer Res.* **2006**, *66* (6), 3317−3322.
(11) Cheng, J.-X.; Xie, X. S. Coherent anti-stokes Raman scattering microscopy: Instrumentation, theory, and applications. *J. Phys. Chem. B* **2004**, *108* (3), 827−840.
(12) Freudiger, C. W.; Min, W.; Saar, B. G.; Lu, S.; Holtom, G. R.; He, C.; Tsai, J. C.; Kang, J. X.; Xie, X. S. Label-free biomedical imaging with high sensitivity by stimulated raman scattering microscopy. *Science* **2008**, *322* (5909), 1857−1861.
(13) Cheng, J.-X.; Xie, X. S. Vibrational spectroscopic imaging of living systems: An emerging platform for biology and medicine. *Science* **2015**, *350* (6264), aaa8870.
(14) Levin, I. W.; Bhargava, R. Fourier transform infrared vibrational spectroscopic imaging: Integrating microscopy and molecular recognition. *Annu. Rev. Phys. Chem.* **2005**, *56* (1), 429−474.
(15) Baker, M. J.; Trevisan, J.; Bassan, P.; Bhargava, R.; Butler, H. J.; Dorling, K. M.; Fielden, P. R.; Fogarty, S. W.; Fullwood, N. J.; Heys, K. A.; Hughes, C.; Lasch, P.; Martin-Hirsch, P. L.; Obinaju, B.; Sockalingum, G. D.; Sulé-Suso, J.; Strong, R. J.; Walsh, M. J.; Wood, B. R.; Gardner, P.; Martin, F. L. Using Fourier transform IR spectroscopy to analyze biological materials. *Nat. Protoc.* **2014**, *9* (8), 1771−1791.
(16) Cheng, J.-X.; Min, W.; Ozeki, Y.; Polli, D. *Stimulated Raman scattering microscopy: Techniques and applications*. Elsevier: **2021**.
(17) Kole, M. R.; Reddy, R. K.; Schulmerich, M. V.; Gelber, M. K.; Bhargava, R. Discrete frequency infrared microspectroscopy and imaging with a tunable quantum cascade laser. *Anal. Chem.* **2012**, *84* (23), 10366−10372.
(18) Dazzi, A.; Prater, C. B.; Hu, Q.; Chase, D. B.; Rabolt, J. F.; Marcott, C. AFM-IR: Combining atomic force microscopy and Infrared spectroscopy for nanoscale chemical characterization. *Appl. Spectrosc.* **2012**, *66* (12), 1365−1384.
(19) Dazzi, A.; Prater, C. B. AFM-IR: Technology and applications in nanoscale infrared spectroscopy and chemical imaging. *Chem. Rev.* **2017**, *117* (7), 5146−5173.
(20) Katzenmeyer, A. M.; Holland, G.; Kjoller, K.; Centrone, A. Absorption spectroscopy and imaging from the visible through mid-infrared with 20 nm resolution. *Anal. Chem.* **2015**, *87* (6), 3154−3159.
(21) Piednoir, A.; Licoppe, C.; Creuzet, F. Imaging and local infrared spectroscopy with a near field optical microscope. *Opt. Commun.* **1996**, *129* (5), 414−422.
(22) Knoll, B.; Keilmann, F. Near-field probing of vibrational absorption for chemical microscopy. *Nature* **1999**, *399* (6732), 134−137.
(23) Huth, F.; Govyadinov, A.; Amarie, S.; Nuansing, W.; Keilmann, F.; Hillenbrand, R. Nano-FTIR absorption spectroscopy of molecular fingerprints at 20 nm spatial resolution. *Nano Lett.* **2012**, *12* (8), 3973−3978.
(24) Perez-Guaita, D.; Kochan, K.; Batty, M.; Doerig, C.; Garcia-Bustos, J.; Espinoza, S.; McNaughton, D.; Heraud, P.; Wood, B. R. Multispectral atomic force microscopy-infrared nano-imaging of malaria infected red blood cells. *Anal. Chem.* **2018**, *90* (5), 3140−3148.
(25) Jin, M.; Lu, F.; Belkin, M. A. High-sensitivity infrared vibrational nanospectroscopy in water. *Light Sci. Appl.* **2017**, *6* (7), e17096−e17096.
(26) Zhang, D.; Li, C.; Zhang, C.; Slipchenko, M. N.; Eakins, G.; Cheng, J.-X. Depth-resolved mid-infrared photothermal imaging of living cells and organisms with submicrometer spatial resolution. *Sci. Adv.* **2016**, *2* (9), No. e1600521.
(27) Bai, Y.; Yin, J.; Cheng, J.-X. Bond-selective imaging by optically sensing the mid-infrared photothermal effect. *Sci. Adv.* **2021**, *7* (20), No. eabg1559.
(28) Schiebener, P.; Straub, J.; Sengers, J. M. H. L.; Gallagher, J. S. Refractive index of water and steam as function of wavelength, temperature and density. *J. Phys. Chem. Ref. Data* **1990**, *19* (3), 677−717.
(29) Fournier, D.; Lepoutre, F.; Boccara, A. Tomographic approach for photothermal imaging using the mirage effect. *J. Phys. Colloques* **1983**, *44* (C6), C6-479−C6-482.
(30) Harada, M.; Iwamoto, K.; Kitamori, T.; Sawada, T. Photothermal microscopy with excitation and probe beams coaxial under the microscope and its application to microparticle analysis. *Anal. Chem.* **1993**, *65* (20), 2938−2940.
(31) Bialkowski, S. E. *Photothermal spectroscopy methods for chemical analysis*; John Wiley & Sons: 1996; Vol. *177*.
(32) Mawatari, K.; Kitamori, T.; Sawada, T. Individual detection of single-nanometer-sized particles in liquid by photothermal microscope. *Anal. Chem.* **1998**, *70* (23), 5037−5041.
(33) Tokeshi, M.; Uchida, M.; Hibara, A.; Sawada, T.; Kitamori, T. Determination of subyoctomole amount of nonfluorescent molecules using a thermal lens microscope: subsingle-molecule determination. *Anal. Chem.* **2001**, *73* (9), 2112−2116.
(34) Adhikari, S.; Spaeth, P.; Kar, A.; Baaske, M. D.; Khatua, S.; Orrit, M. Photothermal microscopy: Imaging the optical absorption of single nanoparticles and single molecules. *ACS Nano* **2020**, *14* (12), 16414−16445.
(35) Boyer, D.; Tamarat, P.; Maali, A.; Lounis, B.; Orrit, M. Photothermal imaging of nanometer-sized metal particles among scatterers. *Science* **2002**, *297* (5584), 1160−1163.
(36) Lasne, D.; Blab, G. A.; De Giorgi, F.; Ichas, F.; Lounis, B.; Cognet, L. Label-free optical imaging of mitochondria in live cells. *Opt. Express* **2007**, *15* (21), 14184−14193.


https://doi.org/10.1021/acs.jpcb.2c05827
J. Phys. Chem. B 2022, 126, 8597−8613

(37) Gaiduk, A.; Yorulmaz, M.; Ruijgrok, P. V.; Orrit, M. Room-temperature detection of a single molecule's absorption by photothermal contrast. *Science* **2010**, *330* (6002), 353−356.
(38) Gaiduk, A.; Ruijgrok, P. V.; Yorulmaz, M.; Orrit, M. Detection limits in photothermal microscopy. *Chem. Sci.* **2010**, *1* (3), 343−350.
(39) Lee, E. S.; Lee, J. Y. Nonlinear optical infrared microscopy with chemical specificity. *Appl. Phys. Lett.* **2009**, *94* (26), 261101.
(40) Lee, E. S.; Lee, J. Y. High resolution cellular imaging with nonlinear optical infrared microscopy. *Opt. Express* **2011**, *19* (2), 1378−1384.
(41) Furstenberg, R.; Kendziora, C. A.; Papantonakis, M. R.; Nguyen, V.; McGill, R. In *Chemical imaging using infrared photothermal microspectroscopy*; Next-Generation Spectroscopic Technologies V, International Society for Optics and Photonics: **2012**; p 837411.
(42) Mërtiri, A.; Jeys, T.; Liberman, V.; Hong, M. K.; Mertz, J.; Altug, H.; Erramilli, S. Mid-infrared photothermal heterodyne spectroscopy in a liquid crystal using a quantum cascade laser. *Appl. Phys. Lett.* **2012**, *101* (4), 044101.
(43) Mertiri, A.; Altug, H.; Hong, M. K.; Mehta, P.; Mertz, J.; Ziegler, L. D.; Erramilli, S. Nonlinear midinfrared photothermal spectroscopy using Zharov splitting and quantum cascade lasers. *ACS Photonics* **2014**, *1* (8), 696−702.
(44) Totachawattana, A.; Liu, H.; Mertiri, A.; Hong, M. K.; Erramilli, S.; Sander, M. Y. Vibrational mid-infrared photothermal spectroscopy using a fiber laser probe: asymptotic limit in signal-to-baseline contrast. *Opt. Lett.* **2016**, *41* (1), 179−182.
(45) Mërtiri, A.; Totachawattana, A.; Hui, L.; Hong, M. K.; Gardner, T.; Sander, M. Y.; Erramilli, S. In Label free mid-IR photothermal imaging of bird brain with quantum cascade laser, *2014 Conference on Lasers and Electro-Optics (CLEO) - Laser Science to Photonic Applications, 8−13 June 2014*; 2014; pp 1−2.
(46) Li, Z.; Kuno, M.; Hartland, G. *Super-resolution imaging with mid-IR photothermal microscopy on the single particle level*. SPIE: **2015**; Vol. *9549*.
(47) Li, C.; Zhang, D.; Slipchenko, M. N.; Cheng, J.-X. Mid-infrared photothermal imaging of active pharmaceutical ingredients at submicrometer spatial resolution. *Anal. Chem.* **2017**, *89* (9), 4863−4867.
(48) Product News. Microscope improves infrared spectroscopy. *J. Fail. Anal. Prev.* **2018**, *18* (2), 250−251.
(49) Li, Z.; Aleshire, K.; Kuno, M.; Hartland, G. V. Super-resolution far-field infrared imaging by photothermal heterodyne imaging. *J. Phys. Chem. B* **2017**, *121* (37), 8838−8846.
(50) Samolis, P. D.; Sander, M. Y. Phase-sensitive lock-in detection for high-contrast mid-infrared photothermal imaging with sub-diffraction limited resolution. *Opt. Express* **2019**, *27* (3), 2643−2655.
(51) Zhang, Y.; Yurdakul, C.; Devaux, A. J.; Wang, L.; Xu, X. G.; Connor, J. H.; Ünlü, M. S.; Cheng, J.-X. Vibrational spectroscopic detection of a single virus by mid-infrared photothermal microscopy. *Anal. Chem.* **2021**, *93* (8), 4100−4107.
(52) Bai, Y.; Zhang, D.; Lan, L.; Huang, Y.; Maize, K.; Shakouri, A.; Cheng, J.-X. Ultrafast chemical imaging by widefield photothermal sensing of infrared absorption. *Sci. Adv.* **2019**, *5* (7), No. eaav7127.
(53) Yin, J.; Lan, L.; Zhang, Y.; Ni, H.; Tan, Y.; Zhang, M.; Bai, Y.; Cheng, J.-X. Nanosecond-resolution photothermal dynamic imaging via MHz digitization and match filtering. *Nat. Commun.* **2021**, *12* (1), 7097.
(54) Zong, H. N.; Yurdakul, C.; Bai, Y. R.; Zhang, M.; Unlu, M. S.; Cheng, J. X. Background-suppressed high-throughput mid-infrared photothermal microscopy via pupil engineering. *ACS Photonics* **2021**, *8* (11), 3323−3336.
(55) Bai, Y.; Zhang, D.; Li, C.; Liu, C.; Cheng, J.-X. Bond-selective imaging of cells by mid-infrared photothermal microscopy in high wavenumber region. *J. Phys. Chem. B* **2017**, *121* (44), 10249−10255.
(56) Yurdakul, C.; Zong, H.; Bai, Y.; Cheng, J.-X.; Selim Ünlü, M. Bond-selective interferometric scattering microscopy. *J. Phys. D* **2021**, *54* (36), 364002.
(57) Zhang, D.; Lan, L.; Bai, Y.; Majeed, H.; Kandel, M. E.; Popescu, G.; Cheng, J.-X. Bond-selective transient phase imaging via sensing of the infrared photothermal effect. *Light Sci. Appl.* **2019**, *8* (1), 116.
(58) Toda, K.; Tamamitsu, M.; Nagashima, Y.; Horisaki, R.; Ideguchi, T. Molecular contrast on phase-contrast microscope. *Sci. Rep.* **2019**, *9* (1), 9957.
(59) Schnell, M.; Mittal, S.; Falahkheirkhah, K.; Mittal, A.; Yeh, K.; Kenkel, S.; Kajdacsy-Balla, A.; Carney, P. S.; Bhargava, R. All-digital histopathology by infrared-optical hybrid microscopy. *Proc. Natl. Acad. Sci. U.S.A.* **2020**, *117* (7), 3388−3396.
(60) Tamamitsu, M.; Toda, K.; Horisaki, R.; Ideguchi, T. Quantitative phase imaging with molecular vibrational sensitivity. *Opt. Lett.* **2019**, *44* (15), 3729−3732.
(61) Tamamitsu, M.; Toda, K.; Shimada, H.; Honda, T.; Takarada, M.; Okabe, K.; Nagashima, Y.; Horisaki, R.; Ideguchi, T. Label-free biochemical quantitative phase imaging with mid-infrared photothermal effect. *Optica* **2020**, *7* (4), 359−366.
(62) Shi, J.; Wong, T. T. W.; He, Y.; Li, L.; Zhang, R.; Yung, C. S.; Hwang, J.; Maslov, K.; Wang, L. V. High-resolution, high-contrast mid-infrared imaging of fresh biological samples with ultraviolet-localized photoacoustic microscopy. *Nat. Photonics* **2019**, *13* (9), 609−615.
(63) Pleitez, M. A.; Khan, A. A.; Soldà, A.; Chmyrov, A.; Reber, J.; Gasparin, F.; Seeger, M. R.; Schätz, B.; Herzig, S.; Scheideler, M.; Ntziachristos, V. Label-free metabolic imaging by mid-infrared optoacoustic microscopy in living cells. *Nat. Biotechnol.* **2020**, *38* (3), 293−296.
(64) Zhang, Y.; Zong, H.; Zong, C.; Tan, Y.; Zhang, M.; Zhan, Y.; Cheng, J.-X. Fluorescence-detected mid-infrared photothermal microscopy. *J. Am. Chem. Soc.* **2021**, *143* (30), 11490−11499.
(65) Li, M.; Razumtcev, A.; Yang, R.; Liu, Y.; Rong, J.; Geiger, A. C.; Blanchard, R.; Pfluegl, C.; Taylor, L. S.; Simpson, G. J. Fluorescence-detected mid-infrared photothermal microscopy. *J. Am. Chem. Soc.* **2021**, *143* (29), 10809−10815.
(66) Razumtcev, A.; Li, M.; Rong, J.; Teng, C. C.; Pfluegl, C.; Taylor, L. S.; Simpson, G. J. Label-free autofluorescence-detected mid-infrared photothermal microscopy of pharmaceutical materials. *Anal. Chem.* **2022**, *94* (17), 6512−6520.
(67) Zhao, J.; Matlock, A.; Zhu, H.; Song, Z.; Zhu, J.; Wang, B.; Chen, F.; Zhan, Y.; Chen, Z.; Xu, Y.; Lin, X.; Tian, L.; Cheng, J.-X., Bond-selective intensity diffraction tomography. *arXiv preprint arXiv:2203.13630* **2022**.
(68) Li, X.; Zhang, D.; Bai, Y.; Wang, W.; Liang, J.; Cheng, J.-X. Fingerprinting a living cell by Raman integrated mid-infrared photothermal microscopy. *Anal. Chem.* **2019**, *91* (16), 10750−10756.
(69) Gustavsson, N.; Paulus, A.; Martinsson, I.; Engdahl, A.; Medjoubi, K.; Klementiev, K.; Somogyi, A.; Deierborg, T.; Borondics, F.; Gouras, G. K.; Klementieva, O. Correlative optical photothermal infrared and X-ray fluorescence for chemical imaging of trace elements and relevant molecular structures directly in neurons. *Light Sci. Appl.* **2021**, *10* (1), 151.
(70) Lima, C.; Muhamadali, H.; Xu, Y.; Kansiz, M.; Goodacre, R. Imaging isotopically labeled bacteria at the single-cell level using high-resolution optical infrared photothermal spectroscopy. *Anal. Chem.* **2021**, *93* (6), 3082−3088.
(71) Xu, J.; Li, X.; Guo, Z.; Huang, W. E.; Cheng, J.-X. Fingerprinting bacterial metabolic response to erythromycin by Raman-integrated mid-infrared photothermal microscopy. *Anal. Chem.* **2020**, *92* (21), 14459−14465.
(72) Aleshire, K.; Pavlovetc, I. M.; Collette, R.; Kong, X.-T.; Rack, P. D.; Zhang, S.; Masiello, D. J.; Camden, J. P.; Hartland, G. V.; Kuno, M. Far-field midinfrared superresolution imaging and spectroscopy of single high aspect ratio gold nanowires. *Proc. Natl. Acad. Sci. U.S.A.* **2020**, *117* (5), 2288−2293.
(73) Su, Y.; Hu, X.; Tang, H.; Lu, K.; Li, H.; Liu, S.; Xing, B.; Ji, R. Steam disinfection releases micro(nano)plastics from silicone-rubber baby teats as examined by optical photothermal infrared microspectroscopy. *Nat. Nanotechnol* **2022**, *17* (1), 76−85.
(74) Pavlovetc, I. M.; Brennan, M. C.; Draguta, S.; Ruth, A.; Moot, T.; Christians, J. A.; Aleshire, K.; Harvey, S. P.; Toso, S.; Nanayakkara,

S. U.; Messinger, J.; Luther, J. M.; Kuno, M. Suppressing cation migration in triple-cation lead halide perovskites. *ACS Energy Lett.* **2020**, *5* (9), 2802−2810.
(75) Berciaud, S.; Cognet, L.; Blab, G. A.; Lounis, B. Photothermal heterodyne imaging of individual nonfluorescent nanoclusters and nanocrystals. *Phys. Rev. Lett.* **2004**, *93* (25), 257402.
(76) Selmke, M.; Heber, A.; Braun, M.; Cichos, F. Photothermal single particle microscopy using a single laser beam. *Appl. Phys. Lett.* **2014**, *105* (1), 013511.
(77) Pavlovetc, I. M.; Aleshire, K.; Hartland, G. V.; Kuno, M. Approaches to mid-infrared, super-resolution imaging and spectroscopy. *Phys. Chem. Chem. Phys.* **2020**, *22* (8), 4313−4325.
(78) Pavlovetc, I. M.; Podshivaylov, E. A.; Chatterjee, R.; Hartland, G. V.; Frantsuzov, P. A.; Kuno, M. Infrared photothermal heterodyne imaging: Contrast mechanism and detection limits. *J. Appl. Phys.* **2020**, *127* (16), 165101.
(79) Bergman, T. L.; Bergman, T. L.; Incropera, F. P.; Dewitt, D. P.; Lavine, A. S. *Fundamentals of heat and mass transfer*; John Wiley & Sons: 2011.
(80) Lim, J. M.; Park, C.; Park, J.-S.; Kim, C.; Chon, B.; Cho, M. Cytoplasmic protein imaging with mid-infrared photothermal microscopy: Cellular dynamics of live neurons and oligodendrocytes. *J. Phys. Chem. Lett.* **2019**, *10* (11), 2857−2861.
(81) Sullenberger, R. M.; Redmond, S. M.; Crompton, D.; Stolyarov, A. M.; Herzog, W. D. Spatially-resolved individual particle spectroscopy using photothermal modulation of Mie scattering. *Opt. Lett.* **2017**, *42* (2), 203−206.
(82) He, Y.; Shi, J.; Pleitez, M.; Maslov, K.; Wagenaar, D.; Wang, L. Label-free imaging of lipid-rich biological tissues by mid-infrared photoacoustic microscopy. *J. Biomed. Opt* **2020**, *25* (10), 106506.
(83) Ortega-Arroyo, J.; Kukura, P. Interferometric scattering microscopy (iSCAT): new frontiers in ultrafast and ultrasensitive optical microscopy. *Phys. Chem. Chem. Phys.* **2012**, *14* (45), 15625−15636.
(84) Zernike, F. Phase contrast, a new method for the microscopic observation of transparent objects. *Physica* **1942**, *9* (10), 974−986.
(85) Toda, K.; Tamamitsu, M.; Ideguchi, T. Adaptive dynamic range shift (ADRIFT) quantitative phase imaging. *Light Sci. Appl.* **2021**, *10* (1), 1.
(86) Quickenden, T. I.; Irvin, J. A. The ultraviolet absorption spectrum of liquid water. *J. Chem. Phys.* **1980**, *72* (8), 4416−4428.
(87) Beaven, G. H.; Holiday, E. R. Ultraviolet absorption spectra of proteins and amino acids. In *Advances in Protein Chemistry*; Anson, M. L., Bailey, K., Edsall, J. T., Eds.; Academic Press: 1952; Vol. 7, pp 319−386..
(88) Wong, T. T. W.; Zhang, R.; Hai, P.; Zhang, C.; Pleitez, M. A.; Aft, R. L.; Novack, D. V.; Wang, L. V. Fast label-free multilayered histology-like imaging of human breast cancer by photoacoustic microscopy. *Sci. Adv.* **2017**, *3* (5), No. e1602168.
(89) Zharov, V. P. Ultrasharp nonlinear photothermal and photoacoustic resonances and holes beyond the spectral limit. *Nat. Photonics* **2011**, *5* (2), 110−116.
(90) He, J.; Miyazaki, J.; Wang, N.; Tsurui, H.; Kobayashi, T. Label-free imaging of melanoma with nonlinear photothermal microscopy. *Opt. Lett.* **2015**, *40* (7), 1141−1144.
(91) Kansiz, M.; Dowling, L. M.; Yousef, I.; Guaitella, O.; Borondics, F.; Sulé-Suso, J. Optical photothermal infrared microspectroscopy discriminates for the first time different types of lung cells on histopathology glass slides. *Anal. Chem.* **2021**, *93* (32), 11081−11088.
(92) Banas, A. M.; Banas, K.; Chu, T. T. T.; Naidu, R.; Hutchinson, P. E.; Agrawal, R.; Lo, M. K. F.; Kansiz, M.; Roy, A.; Chandramohanadas, R.; Breese, M. B. H. Comparing infrared spectroscopic methods for the characterization of Plasmodium falciparum-infected human erythrocytes. *Commun. Chem.* **2021**, *4* (1), 129.
(93) Klementieva, O.; Sandt, C.; Martinsson, I.; Kansiz, M.; Gouras, G. K.; Borondics, F. Super-resolution infrared imaging of polymorphic amyloid aggregates directly in neurons. *Adv. Sci.* **2020**, *7* (6), 1903004.
(94) Spadea, A.; Denbigh, J.; Lawrence, M. J.; Kansiz, M.; Gardner, P. Analysis of fixed and live single cells using optical photothermal infrared with concomitant Raman spectroscopy. *Anal. Chem.* **2021**, *93* (8), 3938−3950.
(95) Bakir, G.; Girouard, B. E.; Wiens, R.; Mastel, S.; Dillon, E.; Kansiz, M.; Gough, K. M. Orientation matters: Polarization dependent IR spectroscopy of collagen from intact tendon down to the single fibril level. *Molecules* **2020**, *25* (18), 4295.
(96) Rahmati, M.; Stötzel, S.; El Khassawna, T.; Mao, C.; Ali, A.; Vaughan, J. C.; Iskhahova, K.; Florian Wieland, D. C.; Cantalapiedra, A. G.; Perale, G.; Betge, F.; Dillon, E. P.; Lyngstadaas, S. P.; Haugen, H. J. Intrinsically disordered peptides enhance regenerative capacities of bone composite xenografts. *Mater. Today* **2022**, *52*, 63.
(97) Khanal, D.; Zhang, J.; Ke, W.-R.; Banaszak Holl, M. M.; Chan, H.-K. Bulk to nanometer-scale infrared spectroscopy of pharmaceutical dry powder aerosols. *Anal. Chem.* **2020**, *92* (12), 8323−8332.
(98) Banas, A.; Banas, K.; Lo, M. K. F.; Kansiz, M.; Kalaiselvi, S. M. P.; Lim, S. K.; Loke, J.; Breese, M. B. H. Detection of high-explosive materials within fingerprints by means of optical-photothermal infrared spectromicroscopy. *Anal. Chem.* **2020**, *92* (14), 9649−9657.
(99) Chatterjee, R.; Pavlovetc, I. M.; Aleshire, K.; Hartland, G. V.; Kuno, M. Subdiffraction infrared imaging of mixed cation perovskites: Probing local cation heterogeneities. *ACS Energy Lett.* **2018**, *3* (2), 469−475.
(100) Marcott, C.; Kansiz, M.; Dillon, E.; Cook, D.; Mang, M. N.; Noda, I. Two-dimensional correlation analysis of highly spatially resolved simultaneous IR and Raman spectral imaging of bioplastics composite using optical photothermal Infrared and Raman spectroscopy. *J. Mol. Struct.* **2020**, *1210*, 128045.
(101) Zhang, A.; Chai, J.; Yang, C.; Zhao, J.; Zhao, G.; Wang, G. Fibrosis mechanism, crystallization behavior and mechanical properties of in-situ fibrillary PTFE reinforced PP composites. *Mater. Des.* **2021**, *211*, 110157.
(102) Olson, N. E.; Xiao, Y.; Lei, Z.; Ault, A. P. Simultaneous optical photothermal infrared (O-PTIR) and Raman spectroscopy of submicrometer atmospheric particles. *Anal. Chem.* **2020**, *92* (14), 9932−9939.
(103) Beltran, V.; Marchetti, A.; Nuyts, G.; Leeuwestein, M.; Sandt, C.; Borondics, F.; De Wael, K. Nanoscale analysis of historical paintings by means of O-PTIR spectroscopy: The identification of the organic particles in L'Arlésienne (Portrait of Madame Ginoux) by Van Gogh. *Angew. Chem., Int. Ed.* **2021**, *60* (42), 22753−22760.
(104) Ma, X.; Pavlidis, G.; Dillon, E.; Beltran, V.; Schwartz, J. J.; Thoury, M.; Borondics, F.; Sandt, C.; Kjoller, K.; Berrie, B. H.; Centrone, A. Micro to nano: Multiscale IR analyses reveal zinc soap heterogeneity in a 19th-century painting by corot. *Anal. Chem.* **2022**, *94* (7), 3103−3110.


https://doi.org/10.1021/acs.jpcb.2c05827
J. Phys. Chem. B 2022, 126, 8597−8613